Inorganic Chemistry

pubs.acs.org/IC

Article

Probing the Origin of Ferro-/Antiferromagnetic Exchange Interactions in Cu(II)−4f Complexes

Naushad Ahmed, Tanu Sharma, Lena Spillecke, Changhyun Koo, Kamal Uddin Ansari, Shalini Tripathi, Andrea Caneschi, Rüdiger Klingeler,* Gopalan Rajaraman,* and Maheswaran Shanmugam*

Cite This: https://doi.org/10.1021/acs.inorgchem.2c00065

Read Online

ACCESS | Metrics & More | Article Recommendations | Supporting Information

ABSTRACT: The mechanistic investigations between Cu(II) and the anisotropic lanthanides (Ln(III)) are not much explored to date. This is due to the complicated energy spectrum which arises due to the orbital angular momentum of anisotropic lanthanides. Interestingly, the exchange coupling J in Ln(III)−Cu(II) systems was found to be antiferromagnetic for <4f^7 metal ions and ferromagnetic for ≥4f^7 metal ions, while the net magnitude of J_{Total} strength gradually decreases moving from f^1 to f^{13}. While this is established in several examples, the reason for this intriguing trend is not rationalized. In this article, we have taken up these challenging tasks by synthesizing a family of complexes with the general molecular formula $[Cu_2Ln(HL)_4(NO_3)](NO_3)_2$, where Ln = La (**1**$_{\text{-La}}$), Ce (**2**$_{\text{-Ce}}$), Pr (**3**$_{\text{-Pr}}$), Gd (**4**$_{\text{-Gd}}$), Tb (**5**$_{\text{-Tb}}$), Dy (**6**$_{\text{-Dy}}$), and Ho (**7**$_{\text{-Ho}}$) and HL = $C_{15}H_{15}N_1O_3$; (2-methoxy-6-[(*E*)-2′-hydroxymethyl-phenyliminomethyl]-phenolate) is a monodeprotonated tridentate Schiff base ligand. Detailed dc magnetic susceptibility measurements performed for all the complexes reveal that the Cu(II) ion is coupled ferromagnetically to the respective Ln(III) ion, which has more than seven electrons in the 4f shell, while an antiferromagnetic coupling is witnessed if Ln(III) has less than seven electrons. The strength of the exchange coupling constant was quantitatively determined for representative complexes from the high-field/high-frequency electron paramagnetic resonance spectroscopy which follows the order of **4**$_{\text{-Gd}}$ (1.50(10) cm^{-1}) > **5**$_{\text{-Tb}}$ (1.18(10) cm^{-1}) > **6**$_{\text{-Dy}}$ (0.56(10) cm^{-1} based on the $-2J_{Cu-Ln}(\overrightarrow{S_{Cu_1}}\cdot\overrightarrow{J^z_{Ln}} + \overrightarrow{S_{Cu_2}}\cdot\overrightarrow{J^z_{Ln}})$ spin Hamiltonian. The increased axiality in **5**$_{\text{-Tb}}$ and **6**$_{\text{-Dy}}$ due to the presence of 3d ions in the near vicinity of an oblate ion and the increased exchange coupling strength between Cu(II) and Tb(III) or Dy(III) is the ideal combination to stabilize magnetic bistability in these complexes in the absence of an external magnetic field with the effective energy barrier of 15.7 K ($\tau_o = 2.49 \times 10^{-6}$ s) and 12.6 K ($\tau_o = 1.70 \times 10^{-5}$ s), respectively. To rationalize this experimental trend, we have performed *ab initio* CASSCF and DFT calculations. To compute the J values, we have employed POLY_ANISO routines and utilized the computed data to establish the generic mechanism of magnetic coupling in {Cu−Ln−Cu} motifs. These mechanistic findings reveal the importance of 5d orbitals and their energy with respect to the $d_{x^2-y^2}$ orbital of Cu(II) ions in controlling the magnetic coupling of {Cu−4f} complexes.

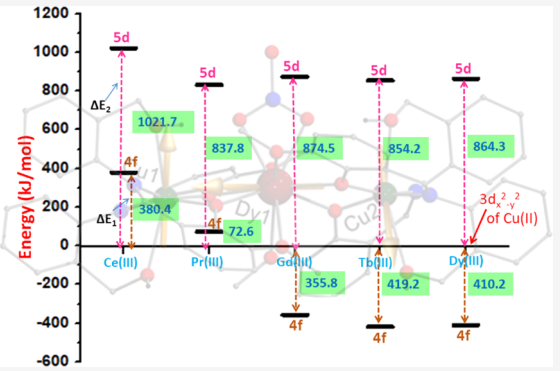

INTRODUCTION

Understanding the mechanism of the exchange interaction between the 3d-ion and 4f-ion is important in many different research areas. Indeed, it modulates the magnetic properties of bulk systems such as spinels, orthoferrites, garnets, magneto-optical devices, permanent magnets (such as Sm_5Co and $Nd_2Fe_{14}B$), high-temperature superconducting materials ($YBa_2Cu_3O_{7-x}$), and so forth.[1−6] Insights of its behavior in 0-dimensional 3d−4f complexes are also a cutting-edge research area currently.[7−27]

The elucidation of the nature of exchange interaction between 3d ion and anisotropic Ln(III) ions (hereafter **Ln(III)**$^{\text{ani}}$) is an extremely challenging task due to the complicated energy-level splitting caused by the unquenched orbital angular momentum coupled with the crystal field around the Ln(III) ions. A further complication arises in these systems, due to the buried nature of 4f-orbitals and hence a weak exchange interaction, which is often masked in the depopulation by M_j sublevels of **Ln(III)**$^{\text{ani}}$ ions. This task then requires a detailed and systematic investigation to develop sound magneto−structural correlations, in analogy to those well established for the complexes containing transition metal ions exclusively.[28−32] Although the empirical approach (*i.e.*

Received: January 11, 2022

substitution of the paramagnetic 3d−4f ion by a suitable diamagnetic analog) developed earlier discloses the overall exchange interaction qualitatively, the investigation related to a quantitative estimate of exchange strength is extremely rare in the literature.[33,34]

In this respect, Ishida, Nojiri, and co-workers have established a method to quantitatively determine the strength of the exchange interaction between the 3d and **Ln(III)^{ani}** ions using high-field/high-frequency electron paramagnetic resonance techniques (HF-EPR).[20,35−38] Besides HF-EPR, other sophisticated analytical techniques such as inelastic neutron scattering,[39] magnetic circular dichroism,[40] high-resolution neutron spectroscopy, and magnetic field dependent far-infrared transmission spectra, have been employed to extract the exchange strength recently.[41−43] On the other hand, the underlying mechanism of the exchange interaction between the 3d and **Ln(III)^{ani}** ions has not been investigated in detail until now. This is a fundamental step to develop magneto-structural correlations in 3d−**Ln(III)^{ani}** complexes because it would provide a rationale for the factors that dictate not only the magnitude but also the sign of exchange interaction (*i.e.,* ferro- or antiferromagnetic interaction).

To shed light on the mechanism of the exchange interaction between 3d−**Ln(III)^{ani}** complexes to develop a magneto-structural correlation, we have investigated a linear hetero-metallic Cu_2Ln series with the general molecular formula of $[Cu_2Ln(HL)_4(NO_3)](NO_3)_2$ where Ln = La (**1**$_{-La}$), Ce (**2**$_{-Ce}$), Pr (**3**$_{-Pr}$), Gd (**4**$_{-Gd}$), Tb (**5**$_{-Tb}$), Dy (**6**$_{-Dy}$), and Ho (**7**$_{-Ho}$) and HL is a monodeprotonated tridentate Schiff base ligand. The detailed dc magnetic studies reveal that the Cu(II) ion is coupled ferromagnetically to Ln(III) ions with a 4f shell, which are either half-filled or more than half-filled, while the nature of exchange coupling is reversed when the Ln(III) ions have less than half-filled electronic configuration. This is in excellent agreement with the results from HF-EPR obtained for the representative 3d−4f metal complexes. Employing *ab initio* CASSCF/DFT calculations, not only the experimental observations are rationalized, but also a generalized mechanism of exchange coupling between the Cu(II) and **Ln(III)^{ani}** ions is proposed. The unique aspect of this finding is that the proposed mechanism for this series can be further generalized to other 3d−4f [where 3d = Fe(II), Co(II), and Ni(II)] complexes.

EXPERIMENTAL SECTION

Unless otherwise mentioned, all the reactions were performed under aerobic conditions. The chemicals were purchased from commercially available sources Alfa Aesar/Sigma-Aldrich and used without further purification. The Schiff base ligand 2-methoxy-6-[(*E*)-2′-hydroxymethyl-phenyliminomethyl]-phenol (**H_2L**) was synthesized by the reported procedure.[44,45] Single crystal data were collected on a Rigaku (Mo Kα, λ = 0.71073 Å). The selected crystals were mounted on a fiber loop using Paratone-N oil and placed in the cold flow produced with an Oxford Cryo-cooling device. Complete hemispheres of data were collected by using ω and φ-scans (0.3 Å, 30 s per frame). Integrated intensities were obtained with SAINT+, and they were corrected for absorption using SADABS.[46] Structure solution and refinement were performed using the SHELX-package.[47] The structures were solved by direct methods and completed by iterative cycles of ΔF syntheses and full-matrix least-squares refinement against F^2. It was not possible to solve the diffused electron density residual which was associated with solvent molecules for all the complexes. This is treated with the SQUEEZE facility from PLATON, resulting in smooth convergence of all the atoms during refinement.[48] CCDC numbers: (2062882−2062888). Powder X-ray data were collected for all the complexes using a powder X-ray diffractometer (PANalytical Netherland, Model: X' Pert Pro, Cu Source, λ = 1.54184 Å). Dc magnetic measurements and magnetic susceptibility measurements were performed on an MPMS-XL SQUID magnetometer (Quantum Design) equipped with a 50 kOe magnet. All the samples were prepared in pellet to avoid orientation of the grains; Pascal's and sample holder's contributions were taken into consideration in the treatment of the data.

All high-frequency/high-field electron paramagnetic resonance (HF-EPR) measurements were performed using a millimeter-wave vector network analyzer (MVNA) from ABmm as a phase-sensitive microwave source and detector and a superconducting magnet from Oxford instruments.[49] Measurements were performed between 80 and 900 GHz, and in magnetic fields up to 16 T. Temperature control between T = 2 and 70 K was ensured by a variable temperature insert with a ^{4}He gas flow cryostat. To enhance signal intensities, the **5**$_{-Tb}$ and **6**$_{-Dy}$ samples were measured as loose powders. They were placed inside a brass ring in a homemade transmission-type EPR probe with no extra glue or grease so that the crystallites were free to align to the external magnetic field direction. To ensure alignment of the loose powder, the maximum magnetic field of B = 16 T was applied before the measurements and the alignment was monitored by observation of corresponding orientation jumps in the transmitted microwave signal. **4**$_{-Gd}$ and **1**$_{-La}$ samples were ground and then fixed with eicosane to avoid partial orientation of the powder. Analysis and simulations of the HF-EPR data were done using the EasySpin software package.[50]

Synthesis of 1$_{-La}$. 2 equiv of the Schiff base ligand **H_2L** (0.2 g, 0.7782 mmol) was treated with 1 equiv sodium methoxide (0.042 g, 0.3889 mmol) in 50 mL of a methanol solvent, and the solution was stirred for a couple of minutes. Into this solution, 1 equiv $La(NO_3)_3\cdot 6H_2O$ (0.158 g, 0.3889 mmol) was added, and the resultant mixture was continued to stir at room temperature for 20 min. Followed by this, 1 equiv of copper acetate hydrate $Cu(CH_3COO)_2\cdot$(0.077 g, 0.3889 mmol) was added. The green solution was further stirred for 24 h, and afterward, the volume was reduced to 2 mL under vacuum. Into that 2 mL of THF solvent (MeOH/THF, 1:1) was added and kept for crystallization at room temperature. The X-ray quality block-shaped crystals were grown in a week by slow evaporation. Yield (based on Cu^{2+}) = 0.141 g (26%), FTIR (KBr pellet): $\nu_{C=N}$ = 1610 cm^{-1}, ν_{Ar-H} = 2923 cm^{-1}.

Synthesis of 2$_{-Ce}$−7$_{-Ho}$. A similar synthetic procedure as described for **1**$_{-La}$ was followed for the isolation of the complexes **2**$_{-Ce}$−**7**$_{-Ho}$, but a corresponding equivalent of $Ln(NO_3)_3\cdot xH_2O$ salt (0.3889 mmol, where Ln = Ce (0.159 g), Pr (0.161 g), Gd (0.133 g), Tb (0.144 g), Dy (0.169 g), or Ho (0.171 g) was used in instead of $La(NO_3)_3\cdot 6H_2O$. The crystals of **4**$_{-Gd}$, which were grown in a MeOH/THF solvent, were found to be not suitable for X-diffraction and were recrystallized in a MeOH/CH_3CN (8 mL; 1:1 ratio) mixture for better quality crystals. Yield of **2**$_{-Ce}$ = 0.140 g (26%), FTIR (KBr pellet): $\nu_{C=N}$ = 1621 cm^{-1}, ν_{Ar-H} = 2941 cm^{-1}. Yield of **3**$_{-Pr}$ = 0.100 g (24%), FTIR (KBr pellet): $\nu_{C=N}$ = 1612 cm^{-1}, ν_{Ar-H} = 2935 cm^{-1}. Yield of **4**$_{-Gd}$ = 0.141 g (26%), FTIR (KBr pellet): $\nu_{C=N}$ = 1621 cm^{-1}, ν_{Ar-H} = 2941 cm^{-1}. Yield of **5**$_{-Tb}$ = 0.140 g (26%), FTIR (KBr pellet): $\nu_{C=N}$ = 1625 cm^{-1}, ν_{Ar-H} = 2944 cm^{-1}. Yield of **6**$_{-Dy}$ = 0.111 g (25%), FTIR (KBr pellet): $\nu_{C=N}$ = 1634 cm^{-1}, ν_{Ar-H} = 2940 cm^{-1} and yield of **7**$_{-Ho}$ = 0.160 g (28%), FTIR (KBr pellet): $\nu_{C=N}$ = 1755 cm^{-1}, ν_{Ar-H} = 2959 cm^{-1} respectively based on Cu.

Note that to confirm the crystalline phase purity of all the complexes, powder X-ray diffraction measurements were performed. The PXRD profile of all the complexes is in good agreement with the simulation pattern generated from their corresponding single-crystal X-ray diffraction structure (Figure S15 of Supporting Information).

RESULTS AND DISCUSSIONS

The reaction of 1 equiv of copper acetate and lanthanide nitrate with 2 equiv of mono deprotonated Schiff base ligand led us to isolate a family of heterometallic trinuclear complexes (see Scheme 1) with the general molecular formula $[Cu_2Ln(HL)_4(NO_3)](NO_3)_2$ {where Ln = La (**1**$_{-La}$), Ce (**2**$_{-Ce}$), Pr

https://doi.org/10.1021/acs.inorgchem.2c00065
Inorg. Chem. XXXX, XXX, XXX−XXX

Scheme 1. General Synthetic Procedure was Followed to Isolate Complexes $\mathbf{1}_{\text{-La}}$–$\mathbf{7}_{\text{-Ho}}$

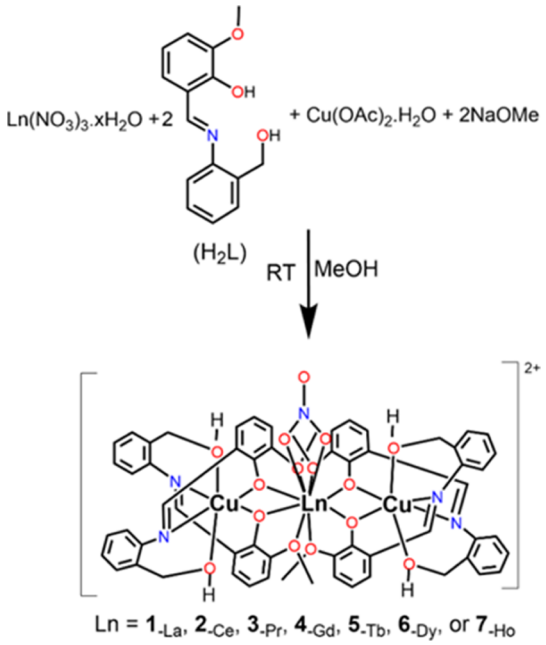

($\mathbf{3}_{\text{-Pr}}$), Gd ($\mathbf{4}_{\text{-Gd}}$), Tb ($\mathbf{5}_{\text{-Tb}}$), Dy ($\mathbf{6}_{\text{-Dy}}$), or Ho ($\mathbf{7}_{\text{-Ho}}$)}. All the complexes crystallized in the monoclinic, $C2/c$ space group except $\mathbf{2}_{\text{-Ce}}$, which is crystallized in the triclinic, $P\bar{1}$ space group (Table S1 of Supporting Information). Consequently, the asymmetric unit (ASU) consists of only half of the molecule for all the complexes except $\mathbf{2}_{\text{-Ce}}$ (Figure 1), and the remaining half of the molecule is generated by a rotation and reflection symmetry. Slight asymmetry around the Cu(II) bond lengths and bond angles in $\mathbf{2}_{\text{-Ce}}$ results in a change in the space group (triclinic, $P\bar{1}$) of this system compared to the other complexes (monoclinic, $C2/c$; *vide infra*). In these complexes, the Ln(III) ion lies in a special position, the C_2-symmetry axis passing through the Ln(III) ion and the N, O atoms of the nitrate anion coordinate to it. The ASU of $\mathbf{2}_{\text{-Ce}}$ consists of the entire molecule (Figure 1A).

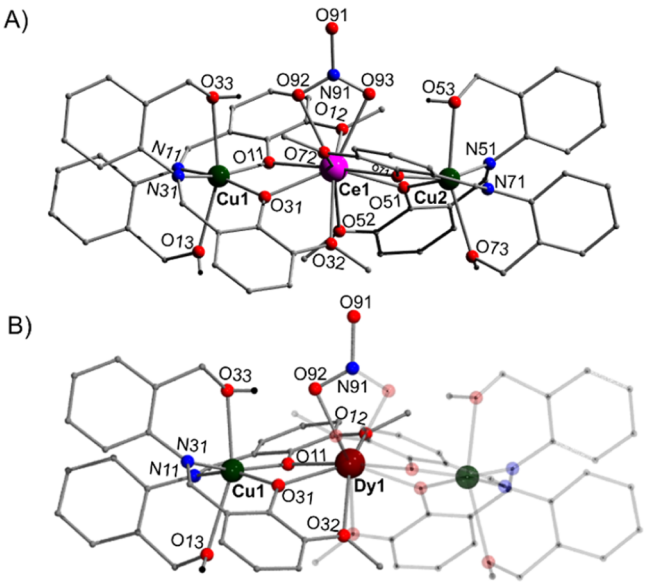

Figure 1. Ball and stick representation of the crystal structure of $\mathbf{2}_{\text{-Ce}}$ (A) and representative complex $\mathbf{6}_{\text{-Dy}}$ (B). The transparent fragment in panel B is generated by a symmetry operation. Color code: red (O), blue (N), gray (C), black (H), dark green (Cu^{II}), wine (Dy^{III}), and magenta (Ce^{III}).

Despite the different space groups, the cationic core of $\mathbf{2}_{\text{-Ce}}$ is structurally analogous to all the other ones, that is a hetero trinuclear complex where the three metal centers are arranged in a near-linear fashion (Cu–Ln–Cu = 169–170°) and the lanthanide ion is sandwiched between the two copper ions. In all the complexes, the Cu(II) ion is surrounded by $\{O_4N_2\}$ donor atoms, which are exclusively derived from two mono-deprotonated Schiff base ligands (**HL**).

Due to the inherent electronic structure associated with the Cu(II) ion, all the copper ions exhibit distorted octahedral geometry owing to the Jahn–Teller distortion. The imino nitrogen atoms and phenoxy donor atoms of HL occupy the equatorial plane of Cu(II) and the axial position is occupied by hydroxymethyl arms of the HL ligands. As expected for a Cu(II) ion with Jahn–Teller elongation, the axial bond lengths (2.3349(1)–2.7118(2) Å) are longer than the equatorial Cu–$N_{(imino)}$ (1.9802(1)–2.070(4) Å) and Cu–$O_{(phenoxo)}$ (1.9396(2)–2.058(1) Å) bond distances.

On the other hand, the Ln(III) ion figures a coordination number of ten. Four methoxo and four phenoxo donor atoms derived from four HL ligands account for the eight out of ten-coordination numbers of the lanthanide ions. The remaining coordination sites of Ln(III) are occupied by a chelating nitrate anion. Thus, the 10-coordinated Ln(III) ion exhibits distorted sphenocorona (C_{2v}) geometry.

The geometry around the lanthanide and copper ions was confirmed by CShM software (Tables S2 and S3 in Supporting Information).[51] In all the complexes, the average bond distance of Ln1–$O_{phenoxo}$ (2.3050(1)–2.5662(1) Å) is shorter than the average Ln1–$O_{methoxo}$ (2.5605(1)–2.6752(1) Å) and the average Ln1–$O_{nitrate}$ bond distance (2.4057(1)–2.5512(1) Å). However, not surprisingly, a uniform trend is naturally observed in all the bond distances, that is, the Ln–O bond distance in each class (phenoxy or methoxy or nitrate), which decreases from $\mathbf{1}_{\text{-La}}$ to $\mathbf{7}_{\text{-Ho}}$, except $\mathbf{4}_{\text{-Gd}}$ due to the lanthanide contraction. The intramolecular Cu(II)···Cu(II) and Cu(II)···Ln(III) bond distance falls in the range of 7.2115(3)–7.0151(2) and 3.6215(2)–3.5202(1) Å, respectively (refer to Table S4 for details).

It is established earlier in the literature that to stabilize Ising magnetic anisotropy in Dy(III) ions, corresponding to an oblate charge distribution on the ion,[52−55] a ligand with high charge density should occupy the axial position. Among the three different coordinating atoms around Dy(III) in $\mathbf{6}_{\text{-Dy}}$, the charge density is expected to be more on the phenoxo donors compared to the nitrate or methoxo ligands. Therefore, the axial direction of the lanthanide is expected to be along the Cu–Dy–Cu axis in this complex. This is consistent with *ab initio* calculations (*vide infra*).

In all the complexes, the Cu(II) and Ln(III) ions are linked through two phenoxo donors of HL ligands exclusively, with an average bond angle of ∠Cu1–O11–Ln1 of 111.3(2)°, while the other angle (∠Cu1–O31–Ln1) is slightly more acute [106.4(3)°] compared to the former one. The presence of only one type of bridging ligand between the Cu(II) and Ln(III) ion is extremely important to maintain the axiality of the Ln(III) ion. The presence of bridging ligands with different charge densities (*e.g.*, phenoxo and carboxylate) leads not only to deviations of the g_{zz} orientation of Ln(III) (from Cu–Ln–

https://doi.org/10.1021/acs.inorgchem.2c00065
Inorg. Chem. XXXX, XXX, XXX–XXX

Cu direction) but also introduces rhombicity, which ultimately enables quantum tunneling of magnetization (*vide infra*).[53]

In all the complexes, two dihedral planes are formed (Cu1−O11−Ln1−O31 and Cu1#−O11#−Ln1−O31#; where # represents the symmetrically generated atoms). The atoms within these are not in the same plane, which is evidently reflected in the dihedral angle, which falls in the range between 13.7(2) and 14.9(6)° for all the complexes. Furthermore, it is noticed that the two dihedral planes in each of the complexes are not co-planar but twisted each other by 29−37°. However, there is no distinct trend observed across all the complexes. The four mono-anionic Schiff base ligand (HL) and a chelating nitrate account for five out of seven cationic charges, resulting in an overall two cationic charge on the coordination sphere. Two nitrate anions reside in the crystal lattice to compensate for the cationic charge on the coordination sphere of the complexes.

A similar coordination environment was observed in the cationic core of $\mathbf{2}_{\text{-Ce}}$ as in $\mathbf{3}_{\text{-Pr}}$−$\mathbf{7}_{\text{-Ho}}$, but a slight change in structural parameters (bond lengths, bond angle, and dihedral angle) due to the lanthanide contraction (Table S4 of Supporting Information). Selected bond lengths, bond angles, dihedral angles, and the angle between the dihedral planes for all the complexes are listed in Table S4 of the Supporting Information. In all the complexes ($\mathbf{1}_{\text{-La}}$−$\mathbf{7}_{\text{-Ho}}$), the solvent molecules (MeOH) that reside in the crystal lattice are heavily disordered due to diffused electron density. Despite diligent efforts modeling this, it failed; therefore, we have used the SQUEEZE routine in Platon software to account for the electron density of these disordered solvent molecules. The closest intermolecular Cu(II)···Cu(II) and Ln···Ln distance observed in $\mathbf{6}_{\text{-Dy}}$ is 8.220(3) and 12.013(2) Å, respectively, while the same in $\mathbf{2}_{\text{-Ce}}$ was observed to be 15.540(2) and 16.116(1) Å, respectively. In all the complexes, the nitrate anion coordinated to Ln(III) and the nitrate anions in the crystal lattice facilitate intra-/intermolecular H-bonding and C−H···O type interactions. Thus, a 3D-supramolecular interaction spreads across the crystal lattice (Figures S1, S2 and Table S5 in Supporting Information).

Direct Current (DC) Magnetic Susceptibility Measurement. Variable temperature magnetic susceptibility measurements were performed on polycrystalline samples of $\mathbf{1}_{\text{-La}}$−$\mathbf{7}_{\text{-Ho}}$ in the temperature range of 300−2.0 K in the presence of an external magnetic field of 1 kOe (Figure 2). A room temperature $\chi_M T$ value of 1.24, 1.79, and 2.45 cm^3 K mol^{-1} for complexes $\mathbf{1}_{\text{-La}}$−$\mathbf{3}_{\text{-Pr}}$ is observed, respectively, which is slightly higher than the expected value for two uncoupled Cu(II) ions (for $\mathbf{1}_{\text{-La}}$) and one Ln(III) ion (g_{Ce} = 6/7, $^2F_{5/2}$; g_{Pr} = 4/5, $^3H_4$) for $\mathbf{2}_{\text{-Ce}}$ and $\mathbf{3}_{\text{-Pr}}$, respectively. This observation is not surprising, as the *g*-value of Cu(II) is usually larger than 2.0. A similar trend was observed for the other complexes ($\mathbf{4}_{\text{-Gd}}$−$\mathbf{7}_{\text{-Ho}}$), that is, the $\chi_M T$ values observed for $\mathbf{4}_{\text{-Gd}}$−$\mathbf{7}_{\text{-Ho}}$ at room temperature are 8.83, 12.93, 15.16, 14.84, and 12.63 cm^3 K mol^{-1}, respectively, which is higher than the theoretically expected value (Table 1).

For $\mathbf{1}_{\text{-La}}$, the $\chi_M T$ value decreases gradually upon decreasing the temperature down to 14 K before it rapidly falls below this temperature. This drop is attributed to the antiferromagnetic superexchange interaction between the two Cu(II) ions *via* the diffused empty orbitals of the diamagnetic La(III) ion. Such a behavior has already been reported in the literature and elegantly explained by Gatteschi and co-workers and others.[56,57] Some of us have also shown that by replacing the large La(III) ion with another diamagnetic ion from an s-block element such as sodium, either a weak or no exchange interaction between the paramagnetic center's ion is observed.[58]

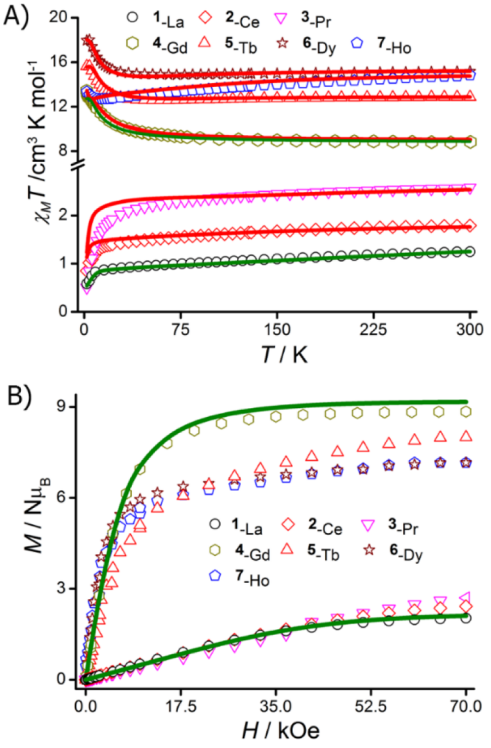

Figure 2. Temperature-dependent magnetic susceptibility plot of a polycrystalline sample of $\mathbf{1}_{\text{-La}}$−$\mathbf{7}_{\text{-Ho}}$ in the presence of an external magnetic field of 1 kOe. (B) Field-dependent magnetization data for all the complexes ($\mathbf{1}_{\text{-La}}$−$\mathbf{7}_{\text{-Ho}}$) measured at 2 K. The solid red line represents the simulation of the experimental data using the parameters described in the main text obtained from POLY_ANISO calculations. The solid green line denotes the simultaneous fit of the experimental magnetic data [$\chi_M T(T)$ and $M(H)$] using the parameters described in the main text.

Table 1. Calculated and Experimentally Observed $\chi_M T$ Value (in cm^3 K mol^{-1}) for Complexes $\mathbf{1}_{\text{-La}}$−$\mathbf{7}_{\text{-Ho}}$

	g		*J*		
complex	Cu	Ln	Ln	$\chi_M T$ cal.	$\chi_M T$ exp
$\mathbf{1}_{\text{-La}}$	2			0.75	1.24
$\mathbf{2}_{\text{-Ce}}$	2	6/7	5/2	1.55	1.79
$\mathbf{3}_{\text{-Pr}}$	2	4/5	4	2.35	2.57
$\mathbf{4}_{\text{-Gd}}$	2	2	7/2	8.62	8.83
$\mathbf{5}_{\text{-Tb}}$	2	3/2	6	12.52	12.93
$\mathbf{6}_{\text{-Dy}}$	2	4/3	15/2	14.87	15.16
$\mathbf{7}_{\text{-Ho}}$	2	5/4	8	14.77	14.84

A similar $\chi_M T(T)$ profile like in $\mathbf{1}_{\text{-La}}$ is observed for $\mathbf{2}_{\text{-Ce}}$ and $\mathbf{3}_{\text{-Pr}}$. The gradual decrease in the $\chi_M T$ value upon lowering the temperature (down to 50 K) in these cases is presumably due to the depopulation of M_J sublevels of Ce(III) and Pr(III) ions and/or intramolecular antiferromagnetic coupling between the two Cu(II) ions and Cu···Ln(III) ions. The sudden drop of the $\chi_M T$ value at temperatures below 50 K for $\mathbf{2}_{\text{-Ce}}$ and $\mathbf{3}_{\text{-Pr}}$ and the approach of a final $\chi_M T$ value of 0.85 and 0.48 cm^3 K mole^{-1} at 2 K, respectively, can be attributed to several factors: (1) intermolecular and/or intramolecular antiferromagnetic cou-

https://doi.org/10.1021/acs.inorgchem.2c00065
Inorg. Chem. XXXX, XXX, XXX−XXX

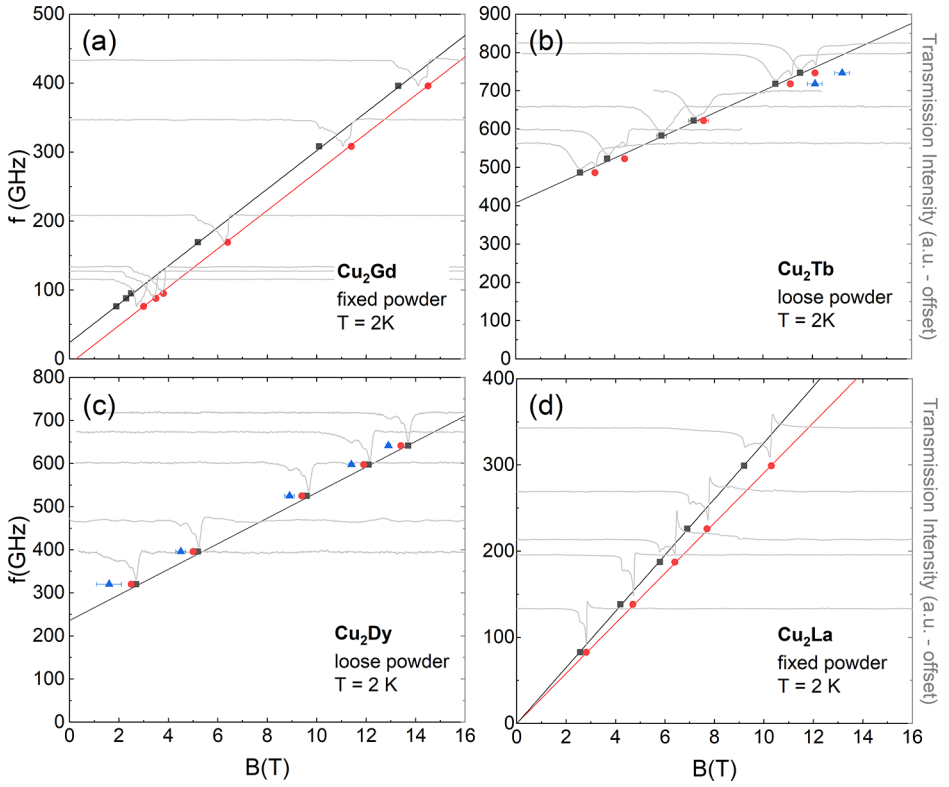

Figure 3. Frequency *vs* resonance field diagram for (a) **4**$_{\text{-Gd}}$, (b) **5**$_{\text{-Tb}}$, (c) **6**$_{\text{-Dy}}$, and (d) **1**$_{\text{-La}}$, at T = 2 K. The magnetic resonance field positions for selected features are marked by different symbols. Solid lines show a simulation or a fit of the field dependence of the selected features using the SH shown in eq 4 (**4**$_{\text{-Gd}}$), eq 5 (**5**$_{\text{-Tb}}$ and **6**$_{\text{-Dy}}$) or an S = 1/2 approach (**1**$_{\text{-La}}$) and the parameters shown in Table 2 or the text. Gray lines display the measured HF-EPR spectra, which are vertically shifted for better comparison with the corresponding resonance positions.

pling, (2) magnetic anisotropy associated with the Ln (III) ions, and (3) dipolar coupling between the molecules.

Unlike complexes **1**$_{\text{-La}}$−**3**$_{\text{-Pr}}$, the $\chi_M T$ value of **4**$_{\text{-Gd}}$ steadily increases upon decreasing the temperature from room temperature down to 40 K. Below this temperature, the $\chi_M T$ value increases rapidly and reaches a maximum value of 13.43 cm^{-3} K mol^{-1} at 4 K. The overall trend noticed for **4**$_{\text{-Gd}}$ is indicative of ferromagnetic exchange interaction between the Cu(II) and Gd(III) ions. The experimentally observed $\chi_M T$ value for **4**$_{\text{-Gd}}$ (13.43 cm^3 K mol^{-1}) at 4 K is slightly higher than the expected $\chi_M T$ value (12.37 cm^3 K mol^{-1}; g = 2) for a well-isolated ground state of 9/2, which is conceivable considering $g_{Cu(II)} > 2$.

For complexes, **5**$_{\text{-Tb}}$−**7**$_{\text{-Ho}}$, a distinctly different trend was noticed compared to **1**$_{\text{-La}}$−**4**$_{\text{-Gd}}$, that is, the $\chi_M T$ value initially decreases gradually from room temperature, but at low temperatures, the $\chi_M T$ value increases to a maximum value. However, the turning point, that is, the temperature at which the $\chi_M T$ value begins to increase for complexes **5**$_{\text{-Tb}}$−**7**$_{\text{-Ho}}$ is distinctly different from one another.

The steady decrease in the $\chi_M T$ value for all the complexes from room temperature is accredited to the depopulation of M_J sublevels of the corresponding Ln(III) ion. The $\chi_M T$ value begins to increase at 66, 47, and 10 K for complexes **5**$_{\text{-Tb}}$−**7**$_{\text{-Ho}}$, respectively.

This implies not only that the Cu(II) ion is showing a ferromagnetic exchange coupling with the corresponding Ln(III) ions in the complexes **5**$_{\text{-Tb}}$−**7**$_{\text{-Ho}}$ but also that the exchange strength decreases as the atomic number increases. This is, in fact, consistent with the exchange coupling constant quantitatively determined from HF-EPR measurements, which are also in excellent agreement with the *ab initio* CASSCF calculations (*vide infra*). Such a scenario has been experimentally proven for certain 3d−4f metal complexes by Krzystek and co-workers through the detailed HF-EPR studies.[12,35,36,59]

Field-dependent magnetization measurements were performed (up to 70 kOe) on polycrystalline samples of **1**$_{\text{-La}}$ to **7**$_{\text{-Ho}}$ at temperatures between 2 and 8 K (Figures 2B and S3 in Supporting Information). The magnetic moment sharply increases as soon as the external magnetic field is turned on for complexes **4**$_{\text{-Gd}}$−**7**$_{\text{-Ho}}$, indicating that the highest m_s or m_j levels are populated. Upon further sweeping the external magnetic field, the magnetic moment tends to saturate at 8.85, 7.99, 7.15, and 7.16 Nμ_B for complexes **4**$_{\text{-Gd}}$−**7**$_{\text{-Ho}}$, respectively. The saturation value close to 9.00 Nμ_B for **4**$_{\text{-Gd}}$ is in excellent agreement with the ground state of 9/2 associated with this complex, while for the other complexes (**5**$_{\text{-Tb}}$−**7**$_{\text{-Ho}}$), the observed magnetic moment is significantly lower than the expected saturation value. This is not surprising for complexes possessing significant magnetic anisotropy. The presence of anisotropy is well corroborated by the nonoverlapping nature of the reduced magnetization curves of these complexes (Figure S4, Supporting Information).

In contrast to the situation observed in **5**$_{\text{-Tb}}$−**7**$_{\text{-Ho}}$, the magnetic moment of **1**$_{\text{-La}}$−**3**$_{\text{-Pr}}$ tends to increase linearly with the external magnetic field, which implies that either the lowest m_j/m_s level or a singlet ground state is populated. The magnetization profile observed for these complexes is consistent with the prediction from empirical methods, that is, the presence of antiferromagnetic interactions between not

https://doi.org/10.1021/acs.inorgchem.2c00065
Inorg. Chem. XXXX, XXX, XXX−XXX

only the two Cu(II) ions but also the Cu(II) and Ce(III) or Pr(III) ions.

To understand the nature/strength of the exchange coupling between the metal ions and the SH parameters associated with the isotropic metal complexes $\mathbf{1}_{\text{-La}}$ and $\mathbf{4}_{\text{-Gd}}$, the experimental magnetic data [both $\chi_M T(T)$ and $M(H)$] were fitted simultaneously[60] using the following Heisenberg exchange Hamiltonian (eq 1).

$$\hat{H} = -2J_1(S_{Cu1}\cdot S_{Gd1} + S_{Cu2}\cdot S_{Gd1}) - 2J_2(S_{Cu1}\cdot S_{Cu2}) \quad (1)$$

For complex $\mathbf{1}_{\text{-La}}$, the first term on the right-hand side of eq 1 is not present. Based on the crystal structure and symmetry present in $\mathbf{4}_{\text{-Gd}}$, we have employed two different exchange coupling constants, J_1 and J_2, which denote, respectively, the nearest neighbor [Cu(II)···Gd(III)] and the next-nearest neighbor [1,3 interaction, *i.e.*, Cu(II)···Cu(II)] exchange coupling constant to fit the experimental magnetic data simultaneously.

A good agreement to the experimental magnetic data [simultaneous fit of $\chi_M T(T)$ and $M(H)$] of $\mathbf{1}_{\text{-La}}$ was obtained upon employing the J_2-value of −0.88 cm^{-1}, while keeping the *g*-value constant as it is derived from HF-EPR (g_{II} = 2.31 and $g_{\perp}$ = 2.09). Similarly, the following SH parameters J_1 = +1.70 cm^{-1} and J_2 = 0.05 cm^{-1} and isotropic *g*-values for Cu(II) and Gd(III) (g_{Cu} = 2.18 and g_{Gd} = 2.0) show an excellent fit [The slightly higher calculated magnetization value as compared to the data (Figure 2B) for $\mathbf{4}_{\text{-Gd}}$ may be due to the contribution of magnetic anisotropy caused by dipolar interaction] to the magnetic data of $\mathbf{4}_{\text{-Gd}}$ [simultaneous fit of $\chi_M T(T)$ and $M(H)$]. This confirms the dominant ferromagnetic exchange coupling between the magnetic moments of the Cu(II) and Gd(III) ions. The parameters extracted from the fitting of magnetic data are in close agreement with the parameters extracted from HF-EPR. We have also noticed that there is no significant change in the magnetic data fit of $\mathbf{4}_{\text{-Gd}}$ even if we ignore J_2, as the strength of 1,3-interaction appears to be extremely weak (compared to J_1). However, the importance of the inclusion of the 1,3-interaction into the magnetic data fit (particularly at low-temperature regime) was rationalized by some of us recently.[61]

High Field and HF-EPR Studies. The high frequency/high field electron paramagnetic resonance (HF-EPR) technique is well suited for the direct determination of SH parameters such as coupling constants or anisotropy parameters.[62−68] On this account, we performed HF-EPR measurements with a variation of the frequency at a fixed temperature (see Figure 3) and variation of temperature at a fixed frequency (see Figures 4 and S6−S9 in Supporting Information), respectively, on fixed ($\mathbf{4}_{\text{-Gd}}$ and $\mathbf{1}_{\text{-La}}$) and oriented loose ($\mathbf{5}_{\text{-Tb}}$ and $\mathbf{6}_{\text{-Dy}}$) powder samples.

For all complexes under investigation, we obtained well-resolved resonance features in the spectra measured at T = 2 K in the accessible field and frequency range, shown as gray lines in the background of Figure 3a−d, respectively. Distinct resonance positions are marked by different symbols corresponding to the resonance branches. Solid lines show a simulation or fit of selected resonance branches using the proper SH shown in eq 4 (for $\mathbf{4}_{\text{-Gd}}$) or eq 5 ($\mathbf{5}_{\text{-Tb}}$ and $\mathbf{6}_{\text{-Dy}}$) and the parameters discussed below for each investigated compound, separately. The HF-EPR data acquired for $\mathbf{1}_{\text{-La}}$ are discussed in terms of an S = 1/2 approach, as will be justified in the following section (vida infra).

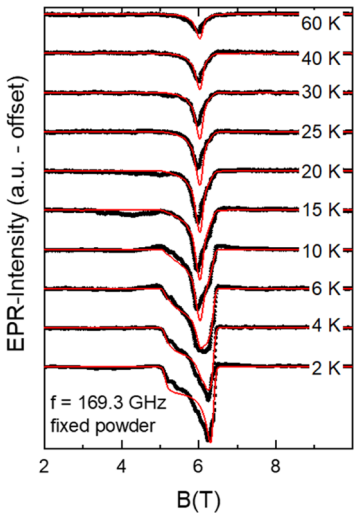

Figure 4. HF-EPR spectra (black symbols) obtained for a fixed powder sample of $\mathbf{4}_{\text{-Gd}}$ at the frequency of f = 169.3 GHz for different temperatures as indicated in the plot. The solid red lines show simulation results using the SH in eq 4 with the parameters shown in Table 2 and the main text.

Figure 3a depicts the frequency versus resonance field diagram for a fixed powder sample of $\mathbf{4}_{\text{-Gd}}$ at T = 2 K. The measured spectra, shown as gray lines in Figure 3a, clearly display a powder-like spectral shape featuring axial anisotropy as it is indicated by the large spectral weight in the high field region of the spectra, while only small spectral weight is observed in the low field region.

Black squares and red dots in Figure 3a mark the low field and high field edges of the corresponding resonance feature, respectively. The edges of the features were used as a reference because the spectra comprise a variety of overlapping transitions (see Figure S5) due to the sample configuration as a fixed powder. Straight lines in Figure 3a show a linear fit to the marked edges. The slope of these fits corresponds to the effective *g*-value of the respective transitions, which amounts to g_{eff} = 2.15(2). Note, that the *g*-value for both selected features is the same, that is, no broadening of the spectra is observed upon increasing the frequencies, which imply at the first glance vanishing *g*-anisotropy on the Cu sites within the resolution of our experiment.

However, even though our experimental data on the slope of the resonance branches do not resolve *g*-anisotropy, a *g*-value significantly larger than the spin-only value implies that a *g*-anisotropy on the Cu sites is likely to be present. Indeed, the measurements on $\mathbf{1}_{\text{-La}}$ (see below) reveal a significant *g*-anisotropy on the Cu(II) sites when the central magnetic Ln ions are replaced by a diamagnetic one. Thus, it can be speculated that the exchange interaction between the Gd(III) and the Cu(II) moments is responsible for the nonresolvable *g*-anisotropy in the EPR data for $\mathbf{4}_{\text{-Gd}}$.

In addition, the data in Figure 3a enable us to obtain two zero-field splitting (ZFS) gaps of 24 GHz (0.8 cm^{-1}) and −7 GHz (−0.23 cm^{-1}) from the intercepts of the black and red lines, respectively. It has been shown in several examples in the literature[49,69] that dipolar interaction can contribute to the anisotropy and thus yield finite ZFS. To rationalize this influence, the dipolar interactions are estimated using the following dipolar Hamiltonian

https://doi.org/10.1021/acs.inorgchem.2c00065
Inorg. Chem. XXXX, XXX, XXX−XXX

$$H_{dip} = S_{Cu1}\vec{D}_{dip}S_{Gd} + S_{Cu2}\vec{D}_{dip}S_{Gd} \quad (2)$$

The dipolar anisotropy tensor $\vec{D}_{dip}$ can be written in the following form[70]

$$\vec{D}_{dip} = \begin{pmatrix} g_{x,Cu}g_{x,Gd}(1 - 3\sin^2\eta\sin^2\xi) & -3g_{x,Gd}g_{y,Cu}\sin^2\xi\sin\eta\cos\eta & -3g_{x,Gd}g_{y,Cu}\sin\xi\sin\eta\cos\xi \\ -3g_{x,Cu}g_{y,Gd}\sin^2\xi\sin\eta\cos\eta & g_{y,Cu}g_{y,Gd}(1 - 3\cos^2\eta\sin^2\xi) & -3g_{x,Gd}g_{y,Cu}\sin\xi\cos\eta\cos\xi \\ -3g_{x,Cu}g_{y,Gd}\sin\xi\cos\xi\sin\eta & -3g_{x,Cu}g_{y,Gd}\sin\xi\cos\xi\cos\eta & g_{z,Cu}g_{z,Gd}(1 - 3\cos^2\xi) \end{pmatrix} \frac{\mu_B^2}{r^3} \quad (3)$$

where r is the distance between the respective Cu and Gd ion and ξ or η define the angle, which is formed by the ionic z- or y-axis and the distant vector $\mathbf{r}$. For the calculations, it is assumed that both Cu(II) ions figure the same g-value $\boldsymbol{g}_{Cu}$ and the anisotropy of $\boldsymbol{g}_{Cu}$ is fixed to the one derived from the HF EPR measurements on the $\mathbf{1}_{\text{-La}}$ sample. $\boldsymbol{g}_{Gd}$ is fixed to the isotropic value of 2.

Figure S12 shows the respective calculated spin projections of the Cu(II) and Gd(III) ions. In a good approximation, it can be assumed that the spin projections of the Gd(III) ion and the Cu(II) ions are perpendicular to each other and thus $\xi = \eta = 0$. Consequently, only the diagonal elements in eq 3 remain finite, which can be quantified to $D^{xx}_{dip} = D^{yy}_{dip} = 0.051$ cm^{-1} and $D^{zz}_{dip} = -0.113$ cm^{-1}. Hence, it can be concluded that a significant dipolar interaction contributes to the anisotropy of the complex.

Figure 4 shows the temperature dependence between $T = 2$ and 60 K of the resonance feature in $\mathbf{4}_{\text{-Gd}}$ at the frequency of 169.3 GHz. At the lowest temperatures, we observe a powder-like spectrum with a sharp peak at $B = 6.2$ T and a shoulder ending at $B = 5$ T. Upon increasing the temperature up to 6 K, the sharp peak starts to broaden and shifts to lower fields. At more elevated temperatures, it sharpens again, while staying at a constant field position of $B = 6$ T. The shoulder on the low field side shifts to higher fields upon heating.

$$H = \mu_B B\vec{g}_{Gd}S_{Gd} + \sum_i^2 \mu_B B\vec{g}_{Cu,i}S_{Cu,i} + \sum_i^2 S_{Cu,i}\vec{D}_{dip}S_{Gd} - 2J_{Cu-Gd}(S_{Cu1}\cdot S_{Gd} + S_{Cu2}\cdot S_{Gd}) - 2J_{Cu-Gd}(S_{Cu1}\cdot S_{Gd} + S_{Cu2}\cdot S_{Gd}) \quad (4)$$

The temperature dependence of the spectra can be simulated using the SH shown in eq 4 where the first and second terms describe the Zeeman effect on the Cu(II) and Gd(III) spins induced by the external magnetic field $\boldsymbol{B}$ and the fourth and fifth term reflects the magnetic interaction between the Cu(II) and Gd(III) spin and the two Cu(II) spins, respectively. The third term describes the dipolar coupling term as it is shown in eq 4.

Red solid lines in Figure 4 show the best simulation results of the temperature-dependent data. The coupling and g-value parameters and their error bars, which were obtained by finding the variation interval in which the simulation gives still a reasonable reproduction of the experimentally observed spectra, are summarized in Table 2. The coupling between the Cu(II) spins described by J_{Cu-Cu} in the last term of eq 4 is fixed to the value obtained by density functional theory (DFT) calculations because an additional coupling parameter would lead to overparameterization. Similarly, to the analysis of the dc magnetization data presented above, $J_{Cu-Cu} = 0$ does not affect the resulting parameters within error bars. The best simulation values for the diagonal elements of the dipolar coupling tensor described in eq 3 are $D^{xx}_{dip} = D^{yy}_{dip} = 0.17(5)$ cm^{-1} and $D^{zz}_{dip} = -0.34(10)$ cm^{-1}, which is in the same range as the calculated values described above. Thus, we conclude that the main contribution to the observed anisotropy is arising from the dipolar interaction of the Gd ions with the two Cu ions. Nevertheless, based on the discrepancy between the calculated and best simulation values, we cannot exclude that there are other contributions to the anisotropy present, which, however, cannot be quantified from the measured data at hand, due to various parameter dependencies in the simulation.

Table 2. SH Parameters Obtained by Simulation of the Temperature Dependence of the Measured HF-EPR Spectra ($\mathbf{4}_{\text{-Gd}}$, See Figure 4) and of the Resonance Branches in the Frequency *vs* Magnetic Field Diagram Using the SH Shown in Equations 4 and 5[a]

	g_{eff}	J_{Ln-Cu} (cm^{-1})	J_{Cu-Cu} (cm^{-1})
$\mathbf{4}_{\text{-Gd}}$ fixed	2.15 (iso) (2.18***)	1.5(10) (1.70***)	−0.25*
$\mathbf{5}_{\text{-Tb}}$ loose	2.08	1.16(5)	±0.33(5)
$\mathbf{6}_{\text{-Dy}}$ loose	2.11	0.58(5)	±0.35(5)
$\mathbf{1}_{\text{-La}}$ fixed	$g_\perp = 2.09(2)$ $g_\parallel = 2.31(2)$		−0.88**

[a]*Value is taken from DFT calculations on $\mathbf{4}_{\text{-Gd}}$ (*cf.* below).**Obtained by PHI fit of the dc magnetization data on $\mathbf{1}_{\text{-La}}$ shown in Figure 2. *** Obtained by PHI fit of the dc magnetization data on $\mathbf{4}_{\text{-Gd}}$ shown in Figure 2.

The resonance features in the powder spectra exhibit a temperature-dependent shift of the intensity toward the center of the spectrum upon heating. This shift can be illustrated and explained by the energy level diagram shown in Figure S5a,b, which correspond to crystallites, where the easy axis of the dipolar tensor is oriented in parallel or perpendicular to the external magnetic field, respectively. For the former (see Figure S5a), the spectral weight shifts to higher fields upon heating, while the opposite is expected for the latter (see Figure S5b).

For $\mathbf{5}_{\text{-Tb}}$ and $\mathbf{6}_{\text{-Dy}}$, oriented loose powder is measured (see the Experimental Section for details). Because the anisotropy of the Ln(III) ions dominates over one of the Cu(II) ions, it is assumed that the crystallites are most likely oriented with the main anisotropy direction $\boldsymbol{d}_{Ln}$ in the local frame of the respective Ln(III) ion along the external magnetic field $\boldsymbol{B}$. Consequently, the measured pseudo-single-crystal spectra consist of contributions arising exclusively from this orientation direction and, hence, only an effective g-value g_{eff} can be measured. In the frequency *vs* magnetic field diagram for $\mathbf{5}_{\text{-Tb}}$ and $\mathbf{6}_{\text{-Dy}}$, two distinct features can be followed over the whole frequency range under study (see Figure 3b,c, respectively). At $T = 2$ K, the most pronounced feature,

https://doi.org/10.1021/acs.inorgchem.2c00065
Inorg. Chem. XXXX, XXX, XXX−XXX

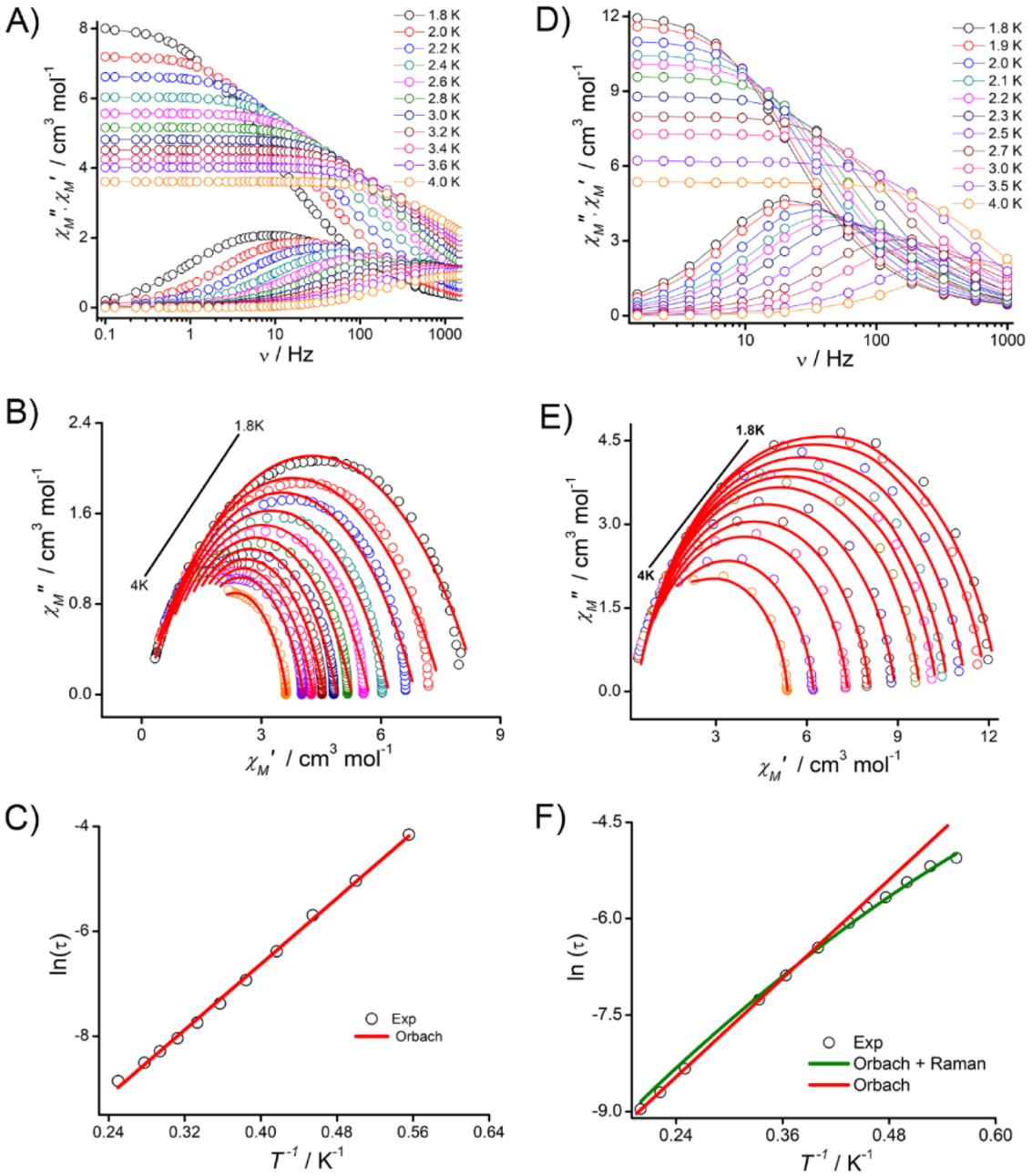

Figure 5. Frequency-dependent ac susceptibility measurements were performed on polycrystalline samples of $\mathbf{5}_{\text{-Tb}}$ and $\mathbf{6}_{\text{-Dy}}$ at the indicated temperatures (H_{ac} = 3.5 Oe) in the absence of an external field. Panels (A–C) represent in-phase/out-of-phase *vs* frequency, Cole–Cole, and the Arrhenius plots, respectively, for the complex $\mathbf{5}_{\text{-Tb}}$, while panels (D–F) correspond to $\mathbf{6}_{\text{-Dy}}$. The solid red curves in panels B and E represent the best fit obtained using the generalized Debye model. The solid red line in panel C and F represent the linear fit, and the solid green line in panel F represent the nonlinear fit (Orbach + Raman) of the experimental data.

marked with black symbols, is attributed to the ground state transition. This assignment is further confirmed by the temperature-dependent measurements (see Figures S6a and S7a), which show that the intensity of the selected features is highest at T = 2 K. Figures S6b and S7b show the temperature dependence of the integrated area over the whole spectra. For both compounds ($\mathbf{5}_{\text{-Tb}}$ and $\mathbf{6}_{\text{-Dy}}$), activated behavior can be observed with a peak around T = 10 K. This indicates the presence of energetically higher states, which are separated from the ground state by more than 10 K and can hence be neglected for discussing the ground state transitions at T = 2 K.

The frequency dependencies of the selected features, assigned as black symbols, for both samples show a linear behavior figuring an effective g-value of g_{eff} = 2.08 and ZFS of 405 GHz for $\mathbf{5}_{\text{-Tb}}$, while g_{eff} = 2.11 and ZFS = 235 GHz for $\mathbf{6}_{\text{-Dy}}$ are observed. Due to the unquenched orbital contribution to the anisotropy of the Ln(III) ions, the separation between the ground and first excited state is much larger than the energy scales of our experiment, so that the Ln(III) moments can be treated as Ising spins.[20,38,59,71] The high axiality of the crystal field is further shown by numerical results discussed in the theoretical section below. Thus, the effective SH considering the Ln ion as Ising spin can be written as

https://doi.org/10.1021/acs.inorgchem.2c00065
Inorg. Chem. XXXX, XXX, XXX–XXX

$$H = \mu_B g_{Ln} B^z J^z_{Ln} + \sum_i^2 \mu_B B \vec{g}_{Cu,i} S_{Cu,i} - 2J_{Cu-Ln}(S^z_{Cu1} \cdot J^z_{Ln} + S^z_{Cu2} \cdot J^z_{Ln}) - 2J_{Cu-Cu} S_{Cu1} \cdot S_{Cu2} \quad (5)$$

As shown in Figure 3, the experimental data are well described by the SH in eq 5. g_{Ln} is thereby fixed to the respective Lande g-value of $g_{Lande} = 3/2$ for Tb(III) or 4/3 for Dy(III). The corresponding energy−level diagrams are shown in Figure S8. In particular, the experimental data do not imply the presence of forbidden transitions with $\Delta m_S > \pm 1$, which corroborates usage of eq 5, that is, approximating J_{Ln} by an Ising spin and neglecting further anisotropy. Hence, the coupling between Ln and Cu moments (J_{Cu-Ln}) can be directly read-off from the ZFS gap of the branches corresponding to the most pronounced feature at low temperatures. The simulation results for **5**$_{\text{-Tb}}$ and **6**$_{\text{-Dy}}$ using the SH in eq 5 are shown as solid black lines in Figure 3b,c, respectively. The J_{Ln-Cu} values amount to 1.16(5) and 0.58(5) cm^{-1} for **5**$_{\text{-Tb}}$ and **6**$_{\text{-Dy}}$, respectively. All parameters used for these simulations are listed in Table 2.

In addition to the main feature, the obtained spectra for **5**$_{\text{-Tb}}$ and **6**$_{\text{-Dy}}$ figure a fine structure in the form of a second feature, which can be followed over the whole measured frequency range, as indicated by the red dots in Figure 3b,c. The appearance of these additional features with a ZFS gap only marginally different from the main branch can be explained if a finite coupling between the Cu ions is considered giving rise to a triplet state. Including $|J_{Cu-Cu}| = 0.33(5)$ and 0.35(5) cm^{-1} for **5**$_{\text{-Tb}}$ and **6**$_{\text{-Dy}}$, respectively, leads to a simulation that perfectly fits the measured data as shown by the red solid lines in Figure 3b,c. These values are in the same range as the J_{Cu-Cu}-values obtained for **4**$_{\text{-Gd}}$ and **1**$_{\text{-La}}$ from DFT calculations or PHI fit, respectively. However, because the relative intensities of the different features are hard to evaluate due to the fact, that both, the orientation of the molecules within the field, as well as other anisotropy effects can have an impact on the very same, conclusions on the *sign* of J_{Cu-Cu} exclusively based on the HF EPR data would be an overinterpretation of our measurement results.

Furthermore, we would like to mention that the explanation of the additional fine structure in the measured spectra by a finite coupling between the Cu(II) ions is, even if well justified by the predictions from dc susceptibility data and DFT calculations, a rather speculative assumption because there are other mechanisms as for example, a mixed ground state of the Ln(III) ion[37] or minimal differences in coupling strength to the two Cu(II) ions, which in principle could also promote additional features.

Investigating **1**$_{\text{-La}}$ enables us to determine the g-anisotropy of the Cu(II) spins in the absence of a Ln(III) moment. The obtained spectra, depicted as gray lines in Figure 3d, show a typical powder-like spectral shape, again figuring axial anisotropy.[72,73] Such anisotropic powder spectra can be described by an $S = 1/2$ approach with an anisotropic g-tensor. The axial symmetry suggests that only the axial ($g_{\parallel}$) and transversal ($g_{\perp}$) contributions of the anisotropic g-tensor need to be considered. The features corresponding to $g_{\parallel}$ and $g_{\perp}$ are marked by red dots and black squares in Figure 3d, respectively. From linear fits to the resonance field positions, we obtain $g_{\parallel} = 2.31(2)$ and $g_{\perp} = 2.09(2)$. Note that there is no ZFS for either branch as expected for a spin S = 1/2 system. The temperature dependence of dc magnetization of **1**$_{\text{-La}}$ shown in Figure 2A implies the presence of a small but finite antiferromagnetic (AFM) coupling between the Cu(II) spins.

However, as demonstrated by the simulation (Figure S9) of the energy-level diagram with the expected transitions shown in Figure S10, the excitation gap induced by this coupling cannot be directly observed by HF-EPR measurements because there is no transition probability between the gapped energy levels. Also, due to the weak coupling, ∼1.3 K, the contribution of a singlet ground state is ignored in our analysis of the HE-EPR data.

Consistent with the literature reports,[35] the exchange strength between Cu−Ln(III) in **4**$_{\text{-Gd}}$, **5**$_{\text{-Tb}}$, and **6**$_{\text{-Dy}}$ complexes decreases gradually. This has been rationalized in the theoretical section below (*vide infra*).

Alternating Current Magnetic Susceptibility Measurements. To investigate the magnetization relaxation dynamics, ac susceptibility measurements were performed for the polycrystalline samples of **5**$_{\text{-Tb}}$−**7**$_{\text{-Ho}}$ in the presence of 3.5 Oe ac oscillating magnetic field. The complex **7**$_{\text{-Ho}}$ shows an out-of-phase susceptibility signal neither in the presence nor in the absence of an external magnetic field (Figure S10 in Supporting Information). This suggests that an under-barrier relaxation mechanism within the ground state (*i.e.* quantum tunneling of magnetization) is dominant compared to the other relaxation processes to reverse the magnetization direction. This scenario is presumably due to the incompatible crystal field around the Ho(III) ion and/or hyperfine interaction, in addition to weak exchange interaction associated with this complex (*vide infra*). In contrast to **7**$_{\text{-Ho}}$, complexes **5**$_{\text{-Tb}}$ and **6**$_{\text{-Dy}}$ show a well-resolved out-of-phase susceptibility signal (χ''_M) that emerges with a concomitant decrease in the in-phase susceptibility signal ($\chi_M{}'$) in the absence of an external magnetic field. Also, the χ''_M signals shift to lower frequencies upon decreasing the temperature. The presence of frequency-dependent χ''_M signals observed for both **5**$_{\text{-Tb}}$ and **6**$_{\text{-Dy}}$ are a characteristic signature of single-molecule magnets (Figure 5). From Figure 5, it is evident that there is only one relaxation process which is reflected in the Cole−Cole plot of both complexes. Considering a single relaxation process (for both **5**$_{\text{-Tb}}$ and **6**$_{\text{-Dy}}$), the Cole−Cole plot was fitted using the Debye equation (eq 6), and the parameters used to fit the data are listed in Tables S6 and S7 in Supporting Information.

$$\chi_s(\omega) = \chi_s + \frac{\chi_T - \chi_s}{1 + (i\omega\tau)^{1-\alpha}} \quad (6)$$

Here, χ_S, χ_T, ω, τ, and α are the adiabatic susceptibility, isothermal susceptibility, angular frequency, relaxation time, and Cole−Cole parameters, respectively. The α-values range from 0.22 to 0.40 for **5**$_{\text{-Tb}}$ and 0.09 to 0.15 for **6**$_{\text{-Dy}}$ which indicates a narrow distribution of relaxation times. The relaxation times extracted from the Cole−Cole fit were used to construct the Arrhenius plot. There is no deviation observed from linearity in the Arrhenius plot in the case of **5**$_{\text{-Tb}}$ (Figure 5C), while in the case of **6**$_{\text{-Dy}}$, a slight deviation appears at low temperature. The latter further reiterates the point that the Orbach process is the predominant relaxation mechanism for the reversal of magnetization orientation compared to the other faster relaxation mechanism such as Raman and QTM. In the case of **5**$_{\text{-Tb}}$ the effective energy barrier extracted from the linear fit of the Arrhenius plot (Figure 5C) is found to be 15.7 K ($\tau_o = 2.49 \times 10^{-6}$ s) for the Orbach process. In the case of **6**$_{\text{-Dy}}$, we have fitted the slightly deviated or nonlinear

https://doi.org/10.1021/acs.inorgchem.2c00065
Inorg. Chem. XXXX, XXX, XXX−XXX

Arrhenius plot using the equation $1/\tau = CT^n + \exp\frac{1}{\tau_0}\left(\frac{-U_{eff}}{K_B T}\right)$ to extract the energy barrier of 12.6 K ($\tau_o = 1.70 \times 10^{-5}$ s) for the Orbach process along with the Raman ($C = 15.14\ s^{-1}\ K^{-3.1}$, $n = 3.1$) relaxation process (Figure 5F). The observed energy barrier for these complexes is comparable to the barrier height reported for structurally similar complexes in the literature (Table S8 of Supporting Information). The routine problem of QTM in Ln(III) containing complexes is not observed in both $\mathbf{5}_{\text{-Tb}}$ and $\mathbf{6}_{\text{-Dy}}$. This can be presumably attributed to the combination of the suitable ligand field around the oblate f-electron configuration and relatively strong exchange interaction between the Cu(II) and Tb(III) or Dy(III) ions.[44,74−76]

Theoretical Studies. To shed light on the electronic structure of the complexes, the influence of magnetic exchange interactions on the magnetization relaxation dynamics, and the mechanism of the exchange interaction between the Cu(II) and the anisotropic lanthanides ion, we have performed CASSCF and DFT calculations. We noticed that the computed $g_{II} > g_{\perp}$ for both the Cu(II) ions in all the complexes (Table S9 of Supporting Information) is consistent with the Jahn−Teller elongated electronic structure and in line with the *g*-tensor extracted from HF-EPR measurements on $\mathbf{1}_{\text{-La}}$. The spin projection on each Cu(II) site in $\mathbf{1}_{\text{-La}}$ is found to be oriented along with the elongated Cu−O(alkoxy) bonds (Jahn Teller axes) and almost perpendicular (85°) to the Cu1−O11−Ln−O31 and Cu1#−O11#−Ln−O31# dihedral planes but they oppose each other. A similar spin projection for the two Cu(II) ions was found in all the complexes ($\mathbf{2}_{\text{-Ce}}$−$\mathbf{7}_{\text{-Ho}}$) as in $\mathbf{1}_{\text{-La}}$ (see Figures 6 and S11).

On the other hand, the magnetization axis on the Ln(III) ion is governed by the charge density on the ligands bound to it. We and others have noticed in 3d−4f metal complexes, however, that (i) bringing a 3d metal ion in the vicinity of an Ln(III) ion facilitates to increase the charge density on the bridging atom, (ii) a uniform charge density on the bridging ligand (*i.e.* one type bridging atoms, examples phenoxo bridges as observed in complexes $\mathbf{2}_{\text{-Ce}}$−$\mathbf{7}_{\text{-Ho}}$) tend to increase the axiality in lanthanides with oblate/prolate f-electron density, (iii) unequal charge density on the bridging ligand arising due to scrambled ligands (phenoxo, carboxylate, nitrates, *etc.*) tends to increase the rhombicity and hence triggers faster magnetization relaxation than anticipated, and (iv) if the 3d metal ion is diamagnetic, then this structural arrangement manifests to mitigate the intermolecular interactions. Consistent with the abovementioned observations, the magnetization axis (g_z) of oblate f-electron configuration containing lanthanides ($\mathbf{2}_{\text{-Ce}}$, $\mathbf{5}_{\text{-Tb}}$−$\mathbf{7}_{\text{-Ho}}$) orients along the Cu−Ln−Cu axis to avoid the repulsion between the electron density on the bridging ligand and f-electrons on the Ln(III).

The high axial nature of Ln(III) ions in $\mathbf{2}_{\text{-Ce}}$ and $\mathbf{5}_{\text{-Tb}}$−$\mathbf{7}_{\text{-Ho}}$ is disclosed in the computed *g*-tensors where $g_z \gg g_x$ and g_y, and the transverse components are negligibly small for ground m_j state (see Tables S10 and S11 of Supporting Information). As a consequence, not only the ground Kramers doublet (KD) ±15/2, but also the first excited KD (±13/2) is found to have negligible admixing with the other excited state KDs in $\mathbf{6}_{\text{-Dy}}$. Similarly, due to the ideal crystal field around the Tb(III) ion in $\mathbf{5}_{\text{-Tb}}$, the tunnel gap (0.001) observed within the ground state m_j levels (±6) is very small, while the bias field produced by Cu(II) and Tb(III) exchange interactions presumably arrest/prevent the fast relaxation through the ground m_j levels. The orientation of the magnetization axis g_z of Ho(III) is along the Cu−Ho−Cu axis, and it has a larger tunnel gap (0.5 cm^{-1}) within the ground state m_j levels compared to that of $\mathbf{5}_{\text{-Tb}}$. Besides, the presence of hyperfine interactions [$I_{Ho} = 7/2$ (100% abundance)] could also manifest a relaxation of the magnetization vector within the ground m_j levels.

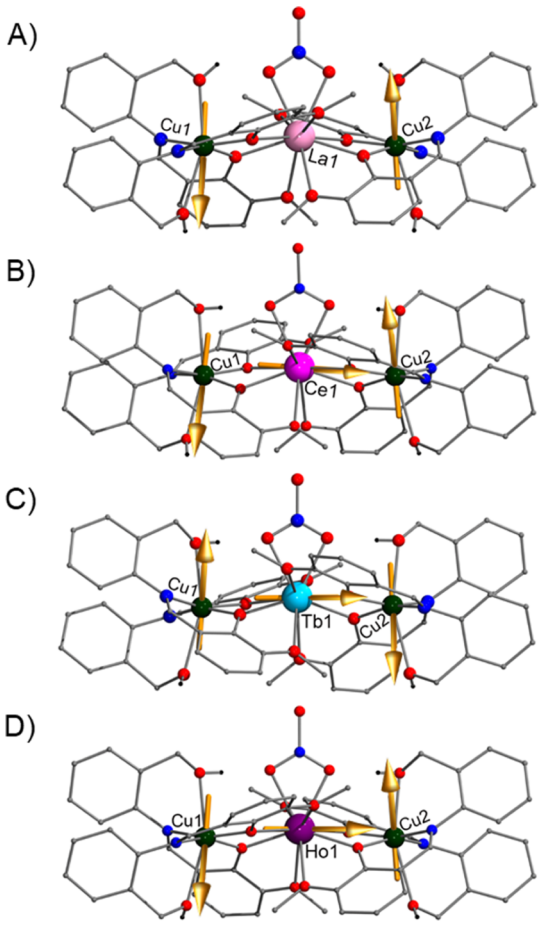

Figure 6. Computed spin projection of Cu1, Cu2, and g_{zz} orientation of Ln(III) ion in their respective complexes. (Here, the *Z*-axis is chosen as the highest order symmetry axis, while the choice of the *X* and *Y* axes is arbitrary).[77,78] The head of the g_{zz} axis is shown only in one direction instead of double-headed arrows to exhibit the nature of the interaction between the metal centers.

Although the wavefunction analysis of SINGLE_ANISO calculations is useful to understand the mechanism of relaxations qualitatively, it does not capture the real scenario as it is an exchange-coupled system. Therefore, we used the ground state wavefunction computed from SINGLE_ANISO as an input file to compute the exchange-coupled energy spectrum using the POLY_ANISO module in the MOLCAS 8.2 suite.[79,80] The resultant energy spectrum was used to explain the experimental trend observed for the magnetization relaxation dynamics of $\mathbf{5}_{\text{-Tb}}$ to $\mathbf{7}_{\text{-Ho}}$. The dc magnetic susceptibility computed from POLY_ANISO for complexes $\mathbf{2}_{\text{-Ce}}$ to $\mathbf{7}_{\text{-Ho}}$ reproduces the experimental magnetic data (Figure 2) and, hence, offers confidence on the extracted SH parameters including the strength of exchange interaction (*J*).

To avoid an over parameterization and to estimate the exchange coupling strength between Cu(II) and the anisotropic lanthanides, we have kept the J_2 value constant at −0.25 cm^{-1} (BS-DFT estimated Cu−Cu interaction in $\mathbf{4}_{\text{-Gd}}$) or 0.0 cm^{-1} for complexes ($\mathbf{4}_{\text{-Gd}}$−$\mathbf{7}_{\text{-Ho}}$), while for $\mathbf{2}_{\text{-Ce}}$ and $\mathbf{3}_{\text{-Pr}}$,

https://doi.org/10.1021/acs.inorgchem.2c00065
Inorg. Chem. XXXX, XXX, XXX−XXX

the Cu(II)···Cu(II) strength (J_2) is fixed at −0.88 cm^{-1} (PHI estimated Cu(II)−Cu(II) interaction in $\mathbf{1}_{\text{-La}}$), and therefore, the lines single parameter approach can be effectively utilized. In line with the prediction from the empirical approach, an antiferromagnetic exchange coupling between Cu (II) and the Ce(III) or Pr(III) ion is witnessed in $\mathbf{2}_{\text{-Ce}}$ (−2.0 cm^{-1}) and $\mathbf{3}_{\text{-Pr}}$ (−1.12 cm^{-1}), respectively. A ferromagnetic exchange coupling constant can be estimated between Cu(II) and the isotropic Gd(III) and anisotropic Ln(III) spins, that is, $J_{\text{Cu-Ln}}$ = +2.40 cm^{-1} (for $\mathbf{4}_{\text{-Gd}}$), +2.30 cm^{-1} (for $\mathbf{5}_{\text{-Tb}}$), +2.15 cm^{-1} (for $\mathbf{6}_{\text{-Dy}}$), and +0.35 cm^{-1} (for $\mathbf{7}_{\text{-Ho}}$).The computed J-values reproduce the experimental trend [*i.e.,* decrease in magnitude of J with increasing atomic number of Ln(III)], which is consistent with experimental observations, although the magnitude of the exchange coupling constants is overestimated. This is in good agreement with the other literature reports as well.[20,35]

To rationalize the experimentally observed dynamic magnetic behaviors, we have analyzed the complete exchange-coupled energy spectrum that arises from the simulation of magnetic data for complexes $\mathbf{5}_{\text{-Tb}}$−$\mathbf{7}_{\text{-Ho}}$ (Figure 7 and see S12 in Supporting Information; also see Tables S12 and S13). To also shed the light on the mechanism of magnetization relaxation dynamics, we have computed the transverse magnetic moment between the connecting pairs of opposing magnetization moment for KD exchange states and the tunneling splitting between non-KD exchange states (Figures 7 and S12 in Supporting Information). The computed tunneling gap Δ_{tun} = 1.0 × 10^{-5} K between the ground state doublet is too low to facilitate the magnetization relaxation between these levels *via* QTM in $\mathbf{5}_{\text{-Tb}}$. Therefore, this complex is expected to show slow relaxation of magnetization in the absence of an external magnetic field. This is in excellent agreement with the experimental observation. Several factors presumably contribute to the zero-field χ''_{M} in $\mathbf{5}_{\text{-Tb}}$: (i) increased axiality due to the presence of 3d-ions in the vicinity of the Tb(III) ion, (ii) small tunnel splitting, and (iii) a relatively strong exchange interaction between the Cu(II) and Tb(III) ion ($J_{\text{Cu-Tb}}$ = +2.30 cm^{-1}). The tunnel splitting (Δ_{tun} = 6.7 × 10^{-4}) for the excited exchange-coupled non-KDs up to the fourth states in complex $\mathbf{5}_{\text{-Tb}}$ was also found to be as low as ≈10^{-4}, which signifies that the relaxation should occur ideally through the fourth excited exchange-coupled state which is separated from the ground-coupled state by 26.5 cm^{-1} or 37.2 K.

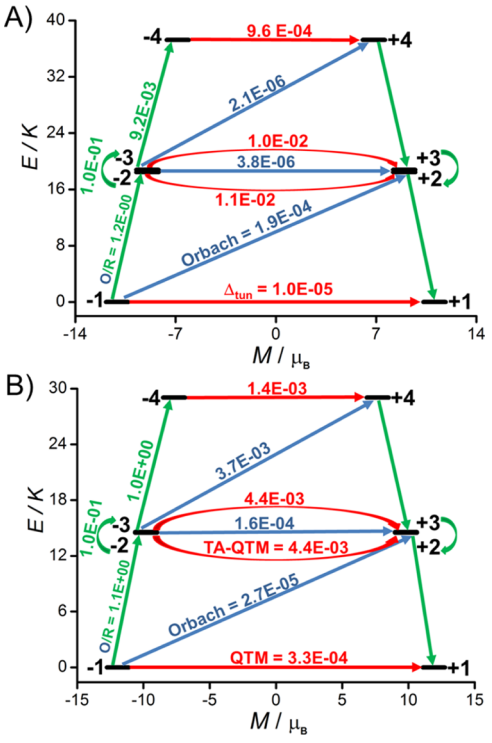

Figure 7. Low-lying non-KDs (A) for $\mathbf{5}_{\text{-Tb}}$ and KDs (B) for $\mathbf{6}_{\text{-Dy}}$ exchange states were obtained from POLY_ANISO simulation. Energy states are placed on the diagram according to their magnetic moment. Red arrows/curves show the tunneling of magnetization within each doublet, while the green and blue arrows show Orbach and Orbach/Raman processes, respectively.

This sets the maximum permissible barrier under extreme dilution conditions. Other excited exchange-coupled states are energetically very high; for instance, the fifth one is separated by 158 cm^{-1} from the ground state (Table S12). The experimentally observed effective energy barrier for complex $\mathbf{5}_{\text{-Tb}}$ of 10.9 cm^{-1} (15.69 K) is in agreement with the computed effective energy barrier of 26.5 cm^{-1} (37.2 K). Similarly, in the case of complex $\mathbf{6}_{\text{-Dy}}$, the transition magnetic moment 3.3 × 10^{-4} μ_{B} between the ground state exchange-coupled KDs, which defines the extent of quantum tunneling of magnetization, is found to be small. This observation is correlated with the linear Arrhenius plot observed for complexes $\mathbf{5}_{\text{-Tb}}$ and $\mathbf{6}_{\text{-Dy}}$ at zero applied dc magnetic field, which shows that the QTM has been suppressed/quenched to the maximum extent. The thermally assisted transition magnetic moment (TA-QTM ≈ 10^{-3}) for up to the fourth low lying excited exchange-coupled states support the relaxation of magnetization through the fourth excited exchange state which is separated by 20.74 cm^{-1} (29.04 K) from the ground state. The experimentally observed zero-field effective energy barrier for complex $\mathbf{6}_{\text{-Dy}}$ was found to be at 8.75 cm^{-1} (12.6 K) and comparable with the computed effective energy barrier for the reversal of magnetization.

The tunnel splitting of 3.3 × 10^{-3} K between the ground exchange state non-KDs in the case of complex $\mathbf{7}_{\text{-Ho}}$ is large (Figures S12 and Table S13 in Supporting Information) and triggers magnetic relaxation within the ground states itself. This rationalizes the absence of any slow relaxation of magnetization (H_{dc} = 0) consistent with experimental observations (Figure S12 in Supporting Information).

Next, we turned our attention to unraveling the mechanism of the exchange interaction between Cu(II) and the anisotropic lanthanide. Before we proceed with the anisotropic system, we have computed the exchange coupling constant for the isotropic $\mathbf{1}_{\text{-La}}$ and $\mathbf{4}_{\text{-Gd}}$ using Noodleman's broken symmetry-DFT (BS-DFT) approach.[81]

To evaluate the exchange coupling constants J_1 and J_2, the following Hamiltonian (eq 7) has been used.

$$\hat{H} = -2[J_1\{(\hat{S}_{\text{Cu1}}\cdot\hat{S}_{\text{Gd}}) + (\hat{S}_{\text{Cu2}}\cdot\hat{S}_{\text{Gd}})\} + J_2(\hat{S}_{\text{Cu1}}\cdot\hat{S}_{\text{Cu2}})] \quad (7)$$

To compute J_1 and J_2, we have considered various BS states (Table S14). The Cu−Gd and Cu1−Cu2 magnetic exchange coupling J_1 and J_2 are found to be +1.69 and −0.25 cm^{-1}, respectively, in complex $\mathbf{4}_{\text{-Gd}}$.

Mechanism of Magnetic Exchange Coupling in {Cu−Ln−Cu}. Based on the detailed experimental and theoretical investigations, the mechanism of magnetic exchange coupling

https://doi.org/10.1021/acs.inorgchem.2c00065
Inorg. Chem. XXXX, XXX, XXX−XXX

within Cu−Gd is well established, and the participation of empty orbitals (5d, 6s, and 6p) for the exchange coupling is invariably accepted. Particularly, the sole antiferromagnetic contribution of the J (J_{AF}) arises from the overlap between $3d_{x^2-y^2}$ and 4f orbitals, while the ferromagnetic contribution to the net exchange (J_F) arises from charge transfer to 5d orbitals or orthogonality between 4f and 3d orbitals.[3,14,19,56,82,83] To analyze various factors mentioned above in **4**$_{-Gd}$, we looked at the symmetry and overlap of the SOMOs. Complex **4**$_{-Gd}$ has an approximate C_{2v} symmetry, and among the seven 4f-orbitals, only two of them have the same irreducible representation to that of Cu(II) $3d_{x^2-y^2}$ orbital and hence could contribute to the antiferromagnetic part of the exchange, while the other five 4f orbitals are expected to be orthogonal to the Cu(II) $3d_{x^2-y^2}$ orbital and hence are expected to contribute to the J_F term. NBO analysis revealed that the electronic configuration of Gd(III) is 6s(0.16)4f(7.01)5d(0.74)6p(0.40), and this shows that the 6s, 5d, and 6p orbitals, which were formally empty orbitals have significant electron occupancy due to polarisation/charge transfer. On the other hand, the literature lacks descriptions of a mechanism for magnetic exchange coupling between Cu−Ln^{ani} ions. In line with the literature reported, we have noticed an antiferromagnetic coupling in **2**$_{-Ce}$ and **3**$_{-Pr}$, while a ferromagnetic coupling is witnessed for **4**$_{-Gd}$−**6**$_{-Dy}$.[20,38] To rationalize the experimentally observed universal trend, not quantitatively but qualitatively, we have performed DFT calculations on complexes **2**$_{-Ce}$, **3**$_{-Pr}$, **4**$_{-Gd}$, **5**$_{-Tb}$, and **6**$_{-Dy}$.

In the pretext of the earlier proposed mechanism for {Cu−Gd}, it is important to underline the overlap between $3d_{x^2-y^2}$ orbital and the 4f orbitals, which is likely to be influenced by their energy difference, that is, a smaller energy difference between these two orbitals may lead to a stronger overlap and, hence, a larger J_{AF} contribution and *vice versa*. Conversely, the scenario that leads to a small energy gap between the $3d_{x^2-y^2}$ orbital and the 5d orbitals of the Ln(III) ions presumably enhances the charge transfer and, hence, has a large J_F contribution to the J_T. Therefore, these two energy gaps could offer further clues into the mechanism of magnetic exchange between the Cu(II) and the anisotropic lanthanide ions.

Henceforth, we have analyzed the energy gap $\Delta E_1 = E_{4f}(Ln) - E_3d_{x^2-y^2}(Cu)$ and $\Delta E_2 = E_{5d}(Ln) - E_3d_{x^2-y^2}(Cu)$ for **2**$_{-Ce}$, **3**$_{-Pr}$, **4**$_{-Gd}$, **5**$_{-Tb}$, and **6**$_{-Dy}$ complexes and plotted their relative energy on the same scale, as shown in Figure 8. It can be seen that, when going from Ce(III) to Pr(III), ΔE_1 decreases from 363.7 to 83.8 kJ/mol and this indicates an increase in J_{AF} to the overall J (J_T) as a smaller gap between these SOMOs. At the same time, ΔE_2 was found to also decrease from 1026 to 868 kJ/mol, indicating that J_F contribution to J_T should strengthen as well (supported by the increase in the energy of 5d orbitals). However, with the exchange contribution being higher for ΔE_1 than for ΔE_2, the net exchange is expected to be antiferromagnetic, but the strength of the J_T is expected to diminish between {Cu−Pr} in **3**$_{-Pr}$ compared to {Cu−Ce} in **2**$_{-Ce}$.

It was further noticed that going from Pr(III) to Gd(III) leads to an increase of ΔE_1 (from 83.8 to 351.6 kJ/mol), which accounts for a decrease in J_{AF} contribution. At the same time, only a marginal increase in ΔE_2 (from 868.4 to 877.5 kJ/mol) leads to an overall ferromagnetic exchange between the Cu−Gd in **4**$_{-Gd}$ as the J_{AF} contribution diminishes significantly. This is consistent with both magnetic and HF-EPR measurements.

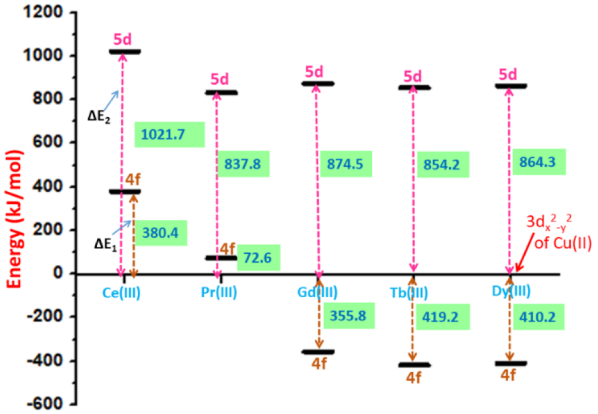

Figure 8. Comparative energies (kJ/mol) of 4f, 5d of Ln(III), and $3d_{x^2-y^2}$ orbital of Cu(II). The energies of Cu(II) $3d_{x^2-y^2}$ are taken as reference for each complexes. The energy differences between 4f(Ln)−$3d_{x^2-y^2}$ (Cu) and 5d(Ln)−$3d_{x^2-y^2}$ (Cu) termed as ΔE_1 and ΔE_2, respectively.

As we move from Gd(III) to the Tb(III) complex, a simple comparison of the energetics of ΔE_1 (a slight increase from 351.6 to 413.7 kJ/mol) and ΔE_2 (a slight decrease from 877.5 to 828.4 kJ/mol) of **5**$_{-Tb}$ with **4**$_{-Gd}$ does not rationalize the experimental trend. Therefore, we have carefully analyzed the overlap integrals in **5**$_{-Tb}$ which are significantly lower for **4**$_{-Gd}$ (implying orbital orthogonality). Careful analysis of **5**$_{-Tb}$ unveils that there is a significant overlap between $4f_{xyz}$ and $3d_{x^2-y^2}$ which is much larger than any other overlap which was computed. This interaction leads to a strong J_{AF} contribution. Due to this J_{AF} contribution to the overall exchange, the net ferromagnetic exchange in **5**$_{-Tb}$ decreases (compared to **4**$_{-Gd}$), which is consistent with the HF-EPR studies.

Again, moving from Tb to Dy, a slight decrease in ΔE_1 and a slight increase in ΔE_2 indicate larger J_{AF} and smaller J_F contributions leading to a drop in the net ferromagnetic exchange compared to Tb(III) as observed. Also, there are three non-zero $\{3d_{x^2-y^2}-4f\}$ overlap integrals for Dy(III) and thus enhancement of the antiferromagnetic contribution leads to a decrease in the net ferromagnetic exchange interactions compared to {Cu−Tb}(Table S15).

To sketch our conclusions, we can say that in the case of less than half-filled lanthanides, small ΔE_1 and less CTC due to large ΔE_2 result in dominant antiferromagnetic Cu−Ln interactions.

When we move from less than half-filled lanthanides to Gd(III), the energies of 4f orbitals of Ln(III) drop compared to that of the Cu(II) $3d_{x^2-y^2}$ orbital. This brings the 5d orbitals of 4f ions close to the Cu(II) $3d_{x^2-y^2}$ (small ΔE_2) leading to a greater J_F contribution. At the same time, ΔE_1 also increases (diminishing J_{AF} contribution), and this ensures not only the change in the magnetic exchange sign but also favors the ferromagnetic exchange interactions (Scheme 2). While the energies qualitatively rationalize the trend observed, it is still important to look at the strength of overlap in some cases as in Tb(III), where an unusually large $|4f_{xyz}|3d_{x^2-y^2}|$ overlap was found, leading to a slight variation from the orbital energy arguments.

In both **4**$_{-Gd}$ and **1**$_{-La}$, the J_2 interaction is estimated to be antiferromagnetic (−0.25 cm^{-1} for **4**$_{-Gd}$ and −0.57 cm^{-1} for **1**$_{-La}$ from DFT calculations). It can be seen that there is a slight difference between the J_2 interactions in **4**$_{-Gd}$ and **1**$_{-La}$, even

https://doi.org/10.1021/acs.inorgchem.2c00065
Inorg. Chem. XXXX, XXX, XXX−XXX

Scheme 2. Proposed Mechanism of Exchange Interaction for Less than Half-Filled (Panel A) and More than Half-Filled Lanthanides (Panel B)[a]

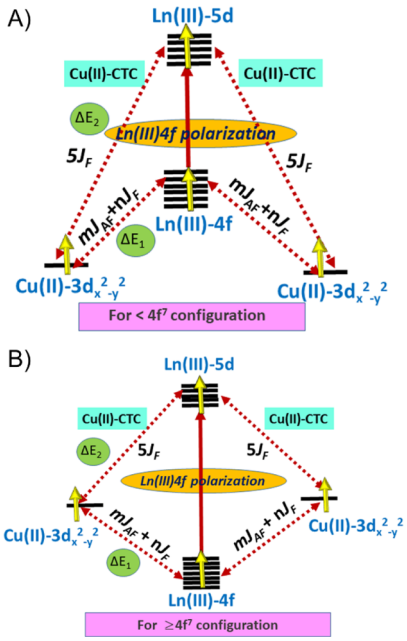

[a]Where J_{AF} represents antiferromagnetic contributions, while J_F represents ferromagnetic contributions to the net exchange interactions. The CTC is charge transfer from Cu(II) $3d_{x^2-y^2}$ orbitals to 5d orbitals of Ln(III); Ln(III) 4f polarization is the polarization of 5d orbitals of Ln(III) by 4f orbitals of Ln(III).

though both these interactions are between the $d_{x^2-y^2}$ orbitals of two Cu(II) ions, which indicates the influence of the electrons in 4f orbitals. The absence of 4f electrons leads to a stronger overlap between the $d_{x^2-y^2}$ orbital of Cu_1 and Cu_2 and thus to a stronger antiferromagnetic interaction in **1**$_{\text{-La}}$ than **4**$_{\text{-Gd}}$. Magneto structural correlations developed earlier for the {Cu−O−Gd} and {Cu−O−Gd−O} dihedral angles affirm that the computed J_1 should be positive and J_2 should be negative, in line with our calculations.[61] The experimentally determined/the computed exchange interaction for the complexes is in good agreement with the complexes reported in the literature which possess similar structural parameters as in **1**$_{\text{-La}}$−**7**$_{\text{-Ho}}$.

CONCLUSIONS

We have isolated a series of near-linear trinuclear Cu−Ln(III)−Cu complexes which are characterized by single-crystal X-ray diffraction with the general molecular formula $[Cu_2Ln(HL)_4(NO_3)](NO_3)_2$, where Ln = La (**1**$_{\text{-La}}$), Ce (**2**$_{\text{-Ce}}$), Pr (**3**$_{\text{-Pr}}$), Gd (**4**$_{\text{-Gd}}$), Tb (**5**$_{\text{-Tb}}$), Dy (**6**$_{\text{-Dy}}$), or Ho (**7**$_{\text{-Ho}}$). The empirical approach followed discloses that an antiferromagnetic coupling dominates between Cu(II) and Ln(III) in **2**$_{\text{-Ce}}$ and **3**$_{\text{-Pr}}$, while a ferromagnetic exchange coupling is dominated between Cu(II) and Ln(III) in the complexes **4**$_{\text{-Gd}}$−**7**$_{\text{-Ho}}$. The turning point moves to a lower temperature from **4**$_{\text{-Gd}}$ to **7**$_{\text{-Ho}}$ in the $\chi_M T(T)$ data, which qualitatively implies that the exchange coupling strength between Cu−Ln(III) decreases in the same order. Strikingly, this experimental trend is confirmed by HF-EPR measurements on representative samples and the ferromagnetic exchange coupling between Cu(II) and Ln(III) is determined with a value of +1.5(10), 1.18(10), 0.56(10) cm^{-1} in **4**$_{\text{-Gd}}$, **5**$_{\text{-Tb}}$, and **6**$_{\text{-Dy}}$, respectively. Remarkably, this experimental observation is well corroborated by computational calculations, that is, not only the calculations predict the correct sign of exchange coupling constant in **1**$_{\text{-La}}$ to **7**$_{\text{-Ho}}$, but also the experimental trend (decrease of ferromagnetic exchange as moving from **4**$_{\text{-Gd}}$ to **7**$_{\text{-Ho}}$) is reproduced. We have identified for the first time the factors that affect the sign and magnitude of exchange coupling between Cu(II) and anisotropic Ln(III) ions. To summarize the finding and the mechanistic aspect in these systems, we notice that the charge transfer from the 3d orbital to the Gd(III) vacant 5d orbital is a dominant factor for the ferromagnetic coupling in **4**$_{\text{-Gd}}$. While the progressive decrease in the magnitude of overall exchange coupling constant from **5**$_{\text{-Tb}}$ to **7**$_{\text{-Ho}}$ (compared to **4**$_{\text{-Gd}}$) is attributed to several parameters, namely, (i) increase in the energy gap between 3d to 5d, (ii) reduced orbital orthogonality, and (iii) increased non-zero orbital overlap (3d and 4f) in complexes **5**$_{\text{-Tb}}$ to **7**$_{\text{-Ho}}$. The ideal crystal field around the oblate ion complexes **5**$_{\text{-Tb}}$ and **6**$_{\text{-Dy}}$ combined with the strong exchange coupling between Cu(II) and Tb(III) or Dy(III), respectively, manifest frequency-dependent out-of-phase susceptibility signals in the absence of zero dc field. While the weak exchange coupling [between Cu(II) and Ho(III)] and the unsuitable crystal field observed for **7**$_{\text{-Ho}}$ facilitates faster relaxation. Therefore, there are no χ''_M signals even in the presence of an external magnetic field. *Ab initio* and DFT calculations suggest that the energy gaps between the $3d_{x^2-y^2}$ and 4f orbitals and the $3d_{x^2-y^2}$ and 5d orbitals of 4f ions are very relevant and dictate the sign and strength of magnetic coupling in the {Cu−Ln} series. In this regard, a hitherto unknown mechanism of magnetic coupling is proposed, which is expected to have implications beyond the examples discussed.

ASSOCIATED CONTENT

Supporting Information

The Supporting Information is available free of charge at https://pubs.acs.org/doi/10.1021/acs.inorgchem.2c00065.

Crystallographic data, supporting magnetic (dc and ac), EPR data, computational details, and energetics of KDs (CCDC numbers: 2062882−2062888) (PDF)

Accession Codes

CCDC 2062882−2062888 contain the supplementary crystallographic data for this paper. These data can be obtained free of charge via www.ccdc.cam.ac.uk/data_request/cif, or by emailing data_request@ccdc.cam.ac.uk, or by contacting The Cambridge Crystallographic Data Centre, 12 Union Road, Cambridge CB2 1EZ, UK; fax: +44 1223 336033.

AUTHOR INFORMATION

Corresponding Authors

Rüdiger Klingeler − *Kirchhoff Institute for Physics, Heidelberg University, 69120 Heidelberg, Germany*; Email: klingeler@kip.uni-heidelberg.de

Gopalan Rajaraman − *Department of Chemistry, Indian Institute of Technology Bombay Powai, Mumbai 400076 Maharashtra, India*; orcid.org/0000-0001-6133-3026; Email: rajaraman@chem.iitb.ac.in

Maheswaran Shanmugam − *Department of Chemistry, Indian Institute of Technology Bombay Powai, Mumbai 400076 Maharashtra, India*; orcid.org/0000-0002-9012-743X; Email: eswar@chem.iitb.ac.in

https://doi.org/10.1021/acs.inorgchem.2c00065
Inorg. Chem. XXXX, XXX, XXX−XXX

Authors

Naushad Ahmed − *Department of Chemistry, Indian Institute of Technology Bombay Powai, Mumbai 400076 Maharashtra, India;* Present Address: Indian Institute of Technology Hyderabad, Kandi, Sangareddy, Telangana 502285, India

Tanu Sharma − *Department of Chemistry, Indian Institute of Technology Bombay Powai, Mumbai 400076 Maharashtra, India*

Lena Spillecke − *Kirchhoff Institute for Physics, Heidelberg University, 69120 Heidelberg, Germany;* orcid.org/0000-0003-0163-6783

Changhyun Koo − *Kirchhoff Institute for Physics, Heidelberg University, 69120 Heidelberg, Germany*

Kamal Uddin Ansari − *Department of Chemistry, Indian Institute of Technology Bombay Powai, Mumbai 400076 Maharashtra, India*

Shalini Tripathi − *Department of Chemistry, Indian Institute of Technology Bombay Powai, Mumbai 400076 Maharashtra, India*

Andrea Caneschi − *Department of Industrial Engineering, "DIEF" and INSTM RU, University of Florence, 50131 Florence, Italy;* orcid.org/0000-0001-5535-3469

Complete contact information is available at: https://pubs.acs.org/10.1021/acs.inorgchem.2c00065

Author Contributions

The manuscript was written through the contributions of all authors.

Notes

The authors declare no competing financial interest.

■ ACKNOWLEDGMENTS

M.S. thanks funding agencies SERB (CRG/2019/004185), CSIR (01(2933)/18/EMR-II), and IIT Bombay for financial support. G.R. thanks DST (DST/SJF/CSA-03/2018-10) and SERB (CRG/2018/000430; SB/SJF/2019-20/12) for funding. G.R. and M.S. thank SERB for SUPRA project (SPR/2019/001145). N.A. is thankful to UGC-India and DST-SERB (PDF/2020/000074) for Fellowships. T.S. is thankful to CSIR India for fellowship. Work at Heidelberg University was supported by BMBF *via* the project *SpinFun* (13XP5088) and by Deutsche Forschungsgemeinschaft (DFG) by project KO5480/1-1 and under Germany's Excellence Strategy EXC2181/1-390900948 (the Heidelberg STRUCTURES Excellence Cluster). L.S. acknowledges support by Landesgraduiertenförderung.

■ REFERENCES

(1) Alsowayigh, M. M.; Timco, G. A.; Borilovic, I.; Alanazi, A.; Vitorica-yrezabal, I. J.; Whitehead, G. F. S.; McNaughter, P. D.; Tuna, F.; O'Brien, P.; Winpenny, R. E. P.; Lewis, D. J.; Collison, D. Heterometallic 3d−4f Complexes as Air-Stable Molecular Precursors in Low Temperature Syntheses of Stoichiometric Rare-Earth Orthoferrite Powders. *Inorg. Chem.* **2020**, *59*, 15796−15806.

(2) Sankar, S. G.; Rao, V. U. S.; Segal, E.; Wallace, W. E.; Frederick, W. G. D.; Garrett, H. J. Magnetocrystalline anisotropy of $SmCo_5$ and its interpretation on a crystal-field model. *Phys. Rev. B: Solid State* **1975**, *11*, 435−439.

(3) Benelli, C.; Caneschi, A.; Gatteschi, D.; Guillou, O.; Pardi, L. Synthesis, crystal structure, and magnetic properties of tetranuclear complexes containing exchange-coupled dilanthanide-dicopper-(lanthanide = gadolinium, dysprosium) species. *Inorg. Chem.* **1990**, *29*, 1750−1755.

(4) Sagawa, M.; Fujimura, S.; Togawa, N.; Yamamoto, H.; Matsuura, Y. New material for permanent magnets on a base of Nd and Fe (invited). *J. Appl. Phys.* **1984**, *55*, 2083−2087.

(5) Kuru, M.; Sahin, O.; Ozarslan, S.; Ozmetin, A. E. Fabrication and mechanical characterization of rare earth permanent magnet SmCo5 films. *J. Alloys Compd.* **2017**, *694*, 726−732.

(6) Hu, D. W.; Yue, M.; Zuo, J. H.; Pan, R.; Zhang, D. T.; Liu, W. Q.; Zhang, J. X.; Guo, Z. H.; Li, W. Structure and magnetic properties of bulk anisotropic SmCo5/α-Fe nanocomposite permanent magnets prepared via a bottom up approach. *J. Alloys Compd.* **2012**, *538*, 173−176.

(7) Dey, A.; Bag, P.; Kalita, P.; Chandrasekhar, V. Heterometallic CuII−LnIII complexes: Single molecule magnets and magnetic refrigerants. *Coord. Chem. Rev.* **2021**, *432*, 213707.

(8) Towatari, M.; Nishi, K.; Fujinami, T.; Matsumoto, N.; Sunatsuki, Y.; Kojima, M.; Mochida, N.; Ishida, T.; Re, N.; Mrozinski, J. Syntheses, Structures, and Magnetic Properties of Acetato- and Diphenolato-Bridged 3d−4f Binuclear Complexes $[M(3\text{-MeOsaltn})(MeOH)_x(ac)Ln(hfac)_2]$ (M = Zn^{II}, Cu^{II}, Ni^{II}, Co^{II}; Ln = La^{III}, Gd^{III}, TbI^{II}, Dy^{III}; 3-MeOsaltn = N,N′-Bis(3-methoxy-2-oxybenzylidene)-1,3-propanediaminato; ac = Acetato; hfac = Hexafluoroacetylacetonato; x = 0 or 1). *Inorg. Chem.* **2013**, *52*, 6160−6178.

(9) Pointillart, F.; Bernot, K.; Sessoli, R.; Gatteschi, D. Effects of 3d−4f Magnetic Exchange Interactions on the Dynamics of the Magnetization of Dy^{III}-M^{II}-Dy^{III} Trinuclear Clusters. *Chem.—Eur. J.* **2007**, *13*, 1602−1609.

(10) Escobar, L. B. L.; Guedes, G. P.; Soriano, S.; Cassaro, R. A. A.; Marbey, J.; Hill, S.; Novak, M. A.; Andruh, M.; Vaz, M. G. F. Synthesis, Crystal Structures, and EPR Studies of First $Mn^{III}Ln^{III}$ Hetero-binuclear Complexes. *Inorg. Chem.* **2018**, *57*, 326−334.

(11) Moreno Pineda, E.; Chilton, N. F.; Tuna, F.; Winpenny, R. E. P.; McInnes, E. J. L. Systematic Study of a Family of Butterfly-Like $\{M_2Ln_2\}$ Molecular Magnets (M = Mg^{II}, Mn^{III}, Co^{II}, Ni^{II}, and Cu^{II}; Ln = Y^{III}, Gd^{III}, Tb^{III}, Dy^{III}, Ho^{III}, and ErI^{II}). *Inorg. Chem.* **2015**, *54*, 5930−5941.

(12) Sorace, L.; Sangregorio, C.; Figuerola, A.; Benelli, C.; Gatteschi, D. Magnetic Interactions and Magnetic Anisotropy in Exchange Coupled 4f−3d Systems: A Case Study of a Heterodinuclear Ce3+−Fe3+ Cyanide-Bridged Complex. *Chem.—Eur. J.* **2009**, *15*, 1377−1388.

(13) Liu, K.; Shi, W.; Cheng, P. Toward heterometallic single-molecule magnets: Synthetic strategy, structures and properties of 3d−4f discrete complexes. *Coord. Chem. Rev.* **2015**, *289*−*290*, 74−122.

(14) Bencini, A.; Benelli, C.; Caneschi, A.; Carlin, R. L.; Dei, A.; Gatteschi, D. Crystal and molecular structure of and magnetic coupling in two complexes containing gadolinium(III) and copper(II) ions. *J. Am. Chem. Soc.* **1985**, *107*, 8128−8136.

(15) Chiboub Fellah, F. Z.; Boulefred, S.; Chiboub Fellah, A.; El Rez, B.; Duhayon, C.; Sutter, J.-P. Binuclear CuLn complexes (LnIII=Gd, Tb, Dy) of alcohol-functionalized bicompartmental Schiff-base ligand. Hydrogen bonding and magnetic behaviors. *Inorg. Chim. Acta* **2016**, *439*, 24−29.

(16) Akine, S.; Matsumoto, T.; Taniguchi, T.; Nabeshima, T. Synthesis, Structures, and Magnetic Properties of Tri- and Dinuclear Copper(II)−Gadolinium(III) Complexes of Linear Oligooxime Ligands. *Inorg. Chem.* **2005**, *44*, 3270−3274.

(17) Kido, T.; Nagasato, S.; Sunatsuki, Y.; Matsumoto, N. A cyclic tetranuclear Cu_2Gd_2 complex with an S = 8 ground state derived from ferromagnetic spin-coupling between copper(ii) and gadolinium(iii) ions arrayed alternately. *Chem. Commun.* **2000**, 2113−2114.

(18) Cirera, J.; Ruiz, E. Exchange coupling in $Cu^{II}Gd^{III}$ dinuclear complexes: A theoretical perspective. *C. R. Chim.* **2008**, *11*, 1227−1234.

(19) Rajaraman, G.; Totti, F.; Bencini, A.; Caneschi, A.; Sessoli, R.; Gatteschi, D. Density functional studies on the exchange interaction of a dinuclear Gd(III)−Cu(II) complex: method assessment,

magnetic coupling mechanism and magneto-structural correlations. *Dalton Trans.* **2009**, 3153−3161.
(20) Shimada, T.; Okazawa, A.; Kojima, N.; Yoshii, S.; Nojiri, H.; Ishida, T. Ferromagnetic Exchange Couplings Showing a Chemical Trend in Cu−Ln−Cu Complexes (Ln = Gd, Tb, Dy, Ho, Er). *Inorg. Chem.* **2011**, *50*, 10555−10557.
(21) Costes, J.-P.; Dahan, F.; Dupuis, A.; Laurent, J.-P. A General Route to Strictly Dinuclear Cu(II)/Ln(III) Complexes. Structural Determination and Magnetic Behavior of Two Cu(II)/Gd(III) Complexes. *Inorg. Chem.* **1997**, *36*, 3429−3433.
(22) Costes, J.-P.; Vendier, L. CuLn complexes with a single μ-oximato bridge. *C. R. Chim.* **2010**, *13*, 661−667.
(23) Costes, J.-P.; Duhayon, C.; Mallet-Ladeira, S.; Shova, S.; Vendier, L. Does the Sign of the Cu−Gd Magnetic Interaction Depend on the Number of Atoms in the Bridge? *Chem.—Eur. J.* **2016**, *22*, 2171−2180.
(24) Costes, J.-P.; Dahan, F.; Dupuis, A. Is Ferromagnetism an Intrinsic Property of the CuII/GdIII Couple? 2. Structures and Magnetic Properties of Novel Trinuclear Complexes with μ-Phenolato-μ-oximato (Cu−Ln−Cu) Cores (Ln = La, Ce, Gd). *Inorg. Chem.* **2000**, *39*, 5994−6000.
(25) Rajeshkumar, T.; Annadata, H. V.; Evangelisti, M.; Langley, S. K.; Chilton, N. F.; Murray, K. S.; Rajaraman, G. Theoretical Studies on Polynuclear $\{Cu^{II}_5Gd^{III}_n\}$ Clusters (n = 4, 2): Towards Understanding Their Large Magnetocaloric Effect. *Inorg. Chem.* **2015**, *54*, 1661−1670.
(26) Kahn, M. L.; Mathonière, C.; Kahn, O. Nature of the Interaction between LnIII and CuII Ions in the Ladder-Type Compounds {Ln2[Cu(opba)]3}·S (Ln = Lanthanide Element; opba = ortho-Phenylenebis(oxamato), S = Solvent Molecules). *Inorg. Chem.* **1999**, *38*, 3692−3697.
(27) Sanz, J. L.; Ruiz, R.; Gleizes, A.; Lloret, F.; Faus, J.; Julve, M.; Borrás-Almenar, J. J.; Journaux, Y. Crystal Structures and Magnetic Properties of Novel $[Ln^{III}Cu^{II}_4]$ (Ln = Gd, Dy, Ho) Pentanuclear Complexes. Topology and Ferromagnetic Interaction in the Ln^{III}−Cu^{II} Pair. *Inorg. Chem.* **1996**, *35*, 7384−7393.
(28) Weihe, H.; Güdel, H. U. Magneto-Structural Correlations in Linear and Bent Oxo-Bridged Transition-Metal Dimers: Comparisons, Interpretations, and Predictions of Ground-State Magnetic Properties. *J. Am. Chem. Soc.* **1998**, *120*, 2870−2879.
(29) Ruiz, E.; Cano, J.; Alvarez, S.; Alemany, P. Magnetic Coupling in End-On Azido-Bridged Transition Metal Complexes: A Density Functional Study. *J. Am. Chem. Soc.* **1998**, *120*, 11122−11129.
(30) Vignesh, K. R.; Langley, S. K.; Gartshore, C. J.; Borilović, I.; Forsyth, C. M.; Rajaraman, G.; Murray, K. S. Rationalizing the sign and magnitude of the magnetic coupling and anisotropy in dinuclear manganese(III) complexes. *Dalton Trans.* **2018**, *47*, 11820−11833.
(31) Khanra, S.; Konar, S.; Clearfield, A.; Helliwell, M.; McInnes, E. J. L.; Tolis, E.; Tuna, F.; Winpenny, R. E. P. Synthesis, Structural and Magnetochemical Studies of Iron Phosphonate Cages Based on $\{Fe_3O\}^{7+}$ Core. *Inorg. Chem.* **2009**, *48*, 5338−5349.
(32) Chang, M.-W.; Gan, P. R.; Peng, Y.-R.; Wu, C.-M.; Huang, Y.-T.; Lee, G.-H.; Chang, C.-K.; Sheu, H.-S.; Yang, E. C. Computational approach for determining the zero-field splitting terms and magnetic coupling strength of in a trigonal Mn_3^{III} complex. *Polyhedron* **2021**, *193*, 114887.
(33) Pasatoiu, T. D.; Sutter, J.-P.; Madalan, A. M.; Fellah, F. Z. C.; Duhayon, C.; Andruh, M. Preparation, Crystal Structures, and Magnetic Features for a Series of Dinuclear $[Ni^{II}Ln^{III}]$ Schiff-Base Complexes: Evidence for Slow Relaxation of the Magnetization for the Dy^{III} Derivative. *Inorg. Chem.* **2011**, *50*, 5890−5898.
(34) Ahmed, N.; Das, C.; Vaidya, S.; Srivastava, A. K.; Langley, S. K.; Murray, K. S.; Shanmugam, M. Probing the magnetic and magnetothermal properties of M(II)−Ln(III) complexes (where M(II) = Ni or Zn; Ln(III) = La or Pr or Gd). *Dalton Trans.* **2014**, *43*, 17375−17384.
(35) Watanabe, R.; Fujiwara, K.; Okazawa, A.; Tanaka, G.; Yoshii, S.; Nojiri, H.; Ishida, T. Chemical trend of Ln−M exchange couplings in heterometallic complexes with Ln = Gd, Tb, Dy, Ho, Er and M = Cu, V. *Chem. Commun.* **2011**, *47*, 2110−2112.
(36) Ida, Y.; Ghosh, S.; Ghosh, A.; Nojiri, H.; Ishida, T. Strong Ferromagnetic Exchange Interactions in Hinge-like $Dy(O_2Cu)_2$ Complexes Involving Double Oxygen Bridges. *Inorg. Chem.* **2015**, *54*, 9543−9555.
(37) Ishida, T.; Watanabe, R.; Fujiwara, K.; Okazawa, A.; Kojima, N.; Tanaka, G.; Yoshii, S.; Nojiri, H. Exchange coupling in TbCu and DyCu single-molecule magnets and related lanthanide and vanadium analogs. *Dalton Trans.* **2012**, *41*, 13609−13619.
(38) Okazawa, A.; Nogami, T.; Nojiri, H.; Ishida, T. Exchange Coupling and Energy-Level Crossing in a Magnetic Chain $[Dy_2Cu_2]n$ Evaluated by High-Frequency Electron Paramagnetic Resonance. *Chem. Mater.* **2008**, *20*, 3110−3119.
(39) Kettles, F. J.; Milway, V. A.; Tuna, F.; Valiente, R.; Thomas, L. H.; Wernsdorfer, W.; Ochsenbein, S. T.; Murrie, M. Exchange Interactions at the Origin of Slow Relaxation of the Magnetization in $\{TbCu_3\}$ and $\{DyCu_3\}$ Single-Molecule Magnets. *Inorg. Chem.* **2014**, *53*, 8970−8978.
(40) Rechkemmer, Y.; Breitgoff, F. D.; van der Meer, M.; Atanasov, M.; Hakl, M.; Orlita, M.; Neugebauer, P.; Neese, F.; Sarkar, B.; van Slageren, J. A four-coordinate cobalt(II) single-ion magnet with coercivity and a very high energy barrier. *Nat. Commun.* **2016**, *7*, 10467.
(41) Kang, T. D.; Standard, E. C.; Rogers, P. D.; Ahn, K. H.; Sirenko, A. A.; Dubroka, A.; Bernhard, C.; Park, S.; Choi, Y. J.; Cheong, S.-W. Far-infrared spectra of the magnetic exchange resonances and optical phonons and their connection to magnetic and dielectric properties of $Dy_3Fe_5O_{12}$ garnet. *Phys. Rev. B: Condens. Matter Mater. Phys.* **2012**, *86*, 144112.
(42) Talbayev, D.; LaForge, A. D.; Trugman, S. A.; Hur, N.; Taylor, A. J.; Averitt, R. D.; Basov, D. N. Magnetic Exchange Interaction between Rare-Earth and Mn Ions in Multiferroic Hexagonal Manganites. *Phys. Rev. Lett.* **2008**, *101*, 247601.
(43) Das, P.; Lin, S.-Z.; Ghimire, N. J.; Huang, K.; Ronning, F.; Bauer, E. D.; Thompson, J. D.; Batista, C. D.; Ehlers, G.; Janoschek, M. Magnitude of the Magnetic Exchange Interaction in the Heavy-Fermion Antiferromagnet $CeRhIn_5$. *Phys. Rev. Lett.* **2014**, *113*, 246403.
(44) Ahmed, N.; Das, C.; Vaidya, S.; Langley, S. K.; Murray, K. S.; Shanmugam, M. Nickel(II)−Lanthanide(III) Magnetic Exchange Coupling Influencing Single-Molecule Magnetic Features in {Ni2Ln2} Complexes. *Chem.—Eur. J.* **2014**, *20*, 14235−14239.
(45) Ahmed, N.; Upadhyay, A.; Rajeshkumar, T.; Vaidya, S.; Schnack, J.; Rajaraman, G.; Shanmugam, M. Carboxylate free μ-oxo bridged ferric wheel with a record exchange coupling. *Dalton Trans.* **2015**, *44*, 18743−18747.
(46) Krause, L.; Herbst-Irmer, R.; Sheldrick, G. M.; Stalke, D. Comparison of silver and molybdenum microfocus X-ray sources for single-crystal structure determination. *J. Appl. Crystallogr.* **2015**, *48*, 3−10.
(47) Sheldrick, G. M. Crystal structure refinement with SHELXL. *Acta Crystallogr., Sect. C: Struct. Chem.* **2015**, *71*, 3−8.
(48) Spek, A. L. PLATON SQUEEZE: a tool for the calculation of the disordered solvent contribution to the calculated structure factors. *Acta Crystallogr., Sect. C: Struct. Chem.* **2015**, *71*, 9−18.
(49) Comba, P.; Großhauser, M.; Klingeler, R.; Koo, C.; Lan, Y.; Müller, D.; Park, J.; Powell, A.; Riley, M. J.; Wadepohl, H. Magnetic Interactions in a Series of Homodinuclear Lanthanide Complexes. *Inorg. Chem.* **2015**, *54*, 11247−11258.
(50) Stoll, S.; Schweiger, A. EasySpin, a comprehensive software package for spectral simulation and analysis in EPR. *J. Magn. Reson.* **2006**, *178*, 42−55.
(51) Pinsky, M.; Avnir, D. Continuous Symmetry Measures. 5. The Classical Polyhedra. *Inorg. Chem.* **1998**, *37*, 5575−5582.
(52) Chilton, N. F.; Collison, D.; McInnes, E. J. L.; Winpenny, R. E. P.; Soncini, A. An electrostatic model for the determination of magnetic anisotropy in dysprosium complexes. *Nat. Commun.* **2013**, *4*, 2551.

https://doi.org/10.1021/acs.inorgchem.2c00065
Inorg. Chem. XXXX, XXX, XXX−XXX

(53) Shukla, P.; Ansari, K. U.; Gao, C.; Vaidya, S.; Tripathi, S.; Kumar, P.; Butcher, R. J.; Overgaard, J.; Shanmugam, M. Influence of anion induced geometry change in Zn(II) on the magnetization relaxation dynamics of Dy(III) in Zn−Dy−Zn complexes. *Dalton Trans.* **2020**, *49*, 10580−10593.
(54) Sun, W.-B.; Yan, P.-F.; Jiang, S.-D.; Wang, B.-W.; Zhang, Y.-Q.; Li, H.-F.; Chen, P.; Wang, Z.-M.; Gao, S. High symmetry or low symmetry, that is the question − high performance Dy(III) single-ion magnets by electrostatic potential design. *Chem. Sci.* **2016**, *7*, 684−691.
(55) Upadhyay, A.; Das, C.; Vaidya, S.; Singh, S. K.; Gupta, T.; Mondol, R.; Langley, S. K.; Murray, K. S.; Rajaraman, G.; Shanmugam, M. Role of the Diamagnetic Zinc(II) Ion in Determining the Electronic Structure of Lanthanide Single-Ion Magnets. *Chem.—Eur. J.* **2017**, *23*, 4903−4916.
(56) Andruh, M.; Ramade, I.; Codjovi, E.; Guillou, O.; Kahn, O.; Trombe, J. C. Crystal structure and magnetic properties of [Ln2Cu4] hexanuclear clusters (where Ln = trivalent lanthanide). Mechanism of the gadolinium(III)-copper(II) magnetic interaction. *J. Am. Chem. Soc.* **1993**, *115*, 1822−1829.
(57) Shiga, T.; Ohba, M.; Ōkawa, H. A Series of Trinuclear CuIIILnIIICuII Complexes Derived from 2,6-Di(acetoacetyl)pyridine: Synthesis, Structure, and Magnetism. *Inorg. Chem.* **2004**, *43*, 4435−4446.
(58) Upadhyay, A.; Das, C.; Meera, S. N.; Langley, S. K.; Murray, K. S.; Shanmugam, M. Synthesis and magnetic properties of a 1-D helical chain derived from a Nickel-Sodium Schiff base complex. *J. Chem. Sci.* **2014**, *126*, 1443−1449.
(59) Schmidt, S. F. M.; Koo, C.; Mereacre, V.; Park, J.; Heermann, D. W.; Kataev, V.; Anson, C. E.; Prodius, D.; Novitchi, G.; Klingeler, R.; Powell, A. K. A Three-Pronged Attack To Investigate the Electronic Structure of a Family of Ferromagnetic Fe_4Ln_2 Cyclic Coordination Clusters: A Combined Magnetic Susceptibility, High-Field/High-Frequency Electron Paramagnetic Resonance, and 57Fe Mössbauer Study. *Inorg. Chem.* **2017**, *56*, 4796−4806.
(60) Chilton, N. F.; Anderson, R. P.; Turner, L. D.; Soncini, A.; Murray, K. S. PHI: A powerful new program for the analysis of anisotropic monomeric and exchange-coupled polynuclear d- and f-block complexes. *J. Comput. Chem.* **2013**, *34*, 1164−1175.
(61) Singh, M. K.; Rajeshkumar, T.; Kumar, R.; Singh, S. K.; Rajaraman, G. Role of (1,3) {Cu-Cu} Interaction on the Magneto-Caloric Effect of Trinuclear $\{Cu^{II}\text{-}Gd^{III}\text{-}Cu^{II}\}$ Complexes: Combined DFT and Experimental Studies. *Inorg. Chem.* **2018**, *57*, 1846−1858.
(62) Spillecke, L.; Tripathi, S.; Koo, C.; Ansari, M.; Vaidya, S.; Rasamsetty, A.; Mallah, T.; Rajaraman, G.; Shanmugam, M.; Klingeler, R. A high-frequency EPR study of magnetic anisotropy and intermolecular interactions of Co(II) ions. *Polyhedron* **2021**, *208*, 115389.
(63) Barra, A.-L.; Brunel, L.-C.; Gatteschi, D.; Pardi, L.; Sessoli, R. High-Frequency EPR Spectroscopy of Large Metal Ion Clusters: From Zero Field Splitting to Quantum Tunneling of the Magnetization. *Acc. Chem. Res.* **1998**, *31*, 460−466.
(64) Idešicová, M.; Titiš, J.; Krzystek, J.; Boča, R. Zero-Field Splitting in Pseudotetrahedral Co(II) Complexes: a Magnetic, High-Frequency and -Field EPR, and Computational Study. *Inorg. Chem.* **2013**, *52*, 9409−9417.
(65) Wu, C.-C.; Datta, S.; Wernsdorfer, W.; Lee, G.-H.; Hill, S.; Yang, E.-C. Studies of magnetic properties and HFEPR of octanuclear manganese single-molecule magnets. *Dalton Trans.* **2010**, *39*, 10160−10168.
(66) Bazhenova, T. A.; Zorina, L. V.; Simonov, S. V.; Mironov, V. S.; Maximova, O. V.; Spillecke, L.; Koo, C.; Klingeler, R.; Manakin, Y. V.; Vasiliev, A. N.; Yagubskii, E. B. The first pentagonal-bipyramidal vanadium(iii) complexes with a Schiff-base N_3O_2 pentadentate ligand: synthesis, structure and magnetic properties. *Dalton Trans.* **2020**, *49*, 15287−15298.
(67) Comba, P.; Daumann, L. J.; Klingeler, R.; Koo, C.; Riley, M. J.; Roberts, A. E.; Wadepohl, H.; Werner, J. Correlation of Structural and Magnetic Properties in a Set of Mononuclear Lanthanide Complexes. *Chem.—Eur. J.* **2018**, *24*, 5319−5330.
(68) Tripathi, S.; Vaidya, S.; Ansari, K. U.; Ahmed, N.; Rivière, E.; Spillecke, L.; Koo, C.; Klingeler, R.; Mallah, T.; Rajaraman, G.; Shanmugam, M. Influence of a Counteranion on the Zero-Field Splitting of Tetrahedral Cobalt(II) Thiourea Complexes. *Inorg. Chem.* **2019**, *58*, 9085−9100.
(69) Baggio, R.; Calvo, R.; Garland, M. T.; Peña, O.; Perec, M.; Rizzi, A. Gadolinium and Neodymium Citrates: Evidence for Weak Ferromagnetic Exchange between Gadolinium(III) Cations. *Inorg. Chem.* **2005**, *44*, 8979−8987.
(70) Bencini, A.; Gatteschi, D. *EPR of Exchange Coupled Systems*; Courier Corporation, 2012.
(71) Komijani, D.; Ghirri, A.; Bonizzoni, C.; Klyatskaya, S.; Moreno-Pineda, E.; Ruben, M.; Soncini, A.; Affronte, M.; Hill, S. Radical-lanthanide ferromagnetic interaction in a Tb^{III} bis-phthalocyaninato complex. *Phys. Rev. Mater.* **2018**, *2*, 024405.
(72) Quintanar, L.; Rivillas-Acevedo, L. Studying Metal Ion−Protein Interactions: Electronic Absorption, Circular Dichroism, and Electron Paramagnetic Resonance. In *Protein-Ligand Interactions: Methods and Applications*; Williams, M. A., Daviter, T., Eds.; Humana Press: Totowa, NJ, 2013; pp 267−297.
(73) Hagen, W. R. EPR spectroscopy as a probe of metal centres in biological systems. *Dalton Trans.* **2006**, 4415−4434.
(74) Rinehart, J. D.; Fang, M.; Evans, W. J.; Long, J. R. A N23−Radical-Bridged Terbium Complex Exhibiting Magnetic Hysteresis at 14 K. *J. Am. Chem. Soc.* **2011**, *133*, 14236−14239.
(75) Das, C.; Upadhyay, A.; Shanmugam, M. Influence of Radicals on Magnetization Relaxation Dynamics of Pseudo-Octahedral Lanthanide Iminopyridyl Complexes. *Inorg. Chem.* **2018**, *57*, 9002−9011.
(76) Langley, S. K.; Wielechowski, D. P.; Vieru, V.; Chilton, N. F.; Moubaraki, B.; Abrahams, B. F.; Chibotaru, L. F.; Murray, K. S. A $\{Cr^{III}{}_2Dy^{III}{}_2\}$ Single-Molecule Magnet: Enhancing the Blocking Temperature through 3d Magnetic Exchange. *Angew. Chem., Int. Ed.* **2013**, *52*, 12014−12019.
(77) Jung, J.; Islam, M. A.; Pecoraro, V. L.; Mallah, T.; Berthon, C.; Bolvin, H. Derivation of Lanthanide Series Crystal Field Parameters From First Principles. *Chem.—Eur. J.* **2019**, *25*, 15112−15122.
(78) Autillo, M.; Islam, M. A.; Jung, J.; Pilmé, J.; Galland, N.; Guerin, L.; Moisy, P.; Berthon, C.; Tamain, C.; Bolvin, H. Crystallographic structure and crystal field parameters in the $[An^{IV}(DPA)_3]^{2-}$ series, An = Th, U, Np, Pu. *Phys. Chem. Chem. Phys.* **2020**, *22*, 14293−14308.
(79) Aquilante, F.; Autschbach, J.; Carlson, R. K.; Chibotaru, L. F.; Delcey, M. G.; De Vico, L.; Fdez Galván, I.; Ferré, N.; Frutos, L. M.; Gagliardi, L.; Garavelli, M.; Giussani, A.; Hoyer, C. E.; Li Manni, G.; Lischka, H.; Ma, D.; Malmqvist, P. Å.; Müller, T.; Nenov, A.; Olivucci, M.; Pedersen, T. B.; Peng, D.; Plasser, F.; Pritchard, B.; Reiher, M.; Rivalta, I.; Schapiro, I.; Segarra-Martí, J.; Stenrup, M.; Truhlar, D. G.; Ungur, L.; Valentini, A.; Vancoillie, S.; Veryazov, V.; Vysotskiy, V. P.; Weingart, O.; Zapata, F.; Lindh, R. Molcas 8: New capabilities for multiconfigurational quantum chemical calculations across the periodic table. *J. Comput. Chem.* **2016**, *37*, 506−541.
(80) Chibotaru, L. F.; Ungur, L.; Soncini, A. The Origin of Nonmagnetic Kramers Doublets in the Ground State of Dysprosium Triangles: Evidence for a Toroidal Magnetic Moment. *Angew. Chem., Int. Ed.* **2008**, *47*, 4126−4129.
(81) Noodleman, L. Valence bond description of antiferromagnetic coupling in transition metal dimers. *J. Chem. Phys.* **1981**, *74*, 5737−5743.
(82) O'Connor, C. J. *Research Frontiers in Magnetochemistry*; World Scientific, 1993.
(83) Bencini, A.; Benelli, C.; Caneschi, A.; Dei, A.; Gatteschi, D. Crystal and molecular structure and magnetic properties of a trinuclear complex containing exchange-coupled $GdCu_2$ species. *Inorg. Chem.* **1986**, *25*, 572−575.

https://doi.org/10.1021/acs.inorgchem.2c00065
Inorg. Chem. XXXX, XXX, XXX−XXX